Title

Charge Transport, Spin Transport and Magneto-Optics of Solid-State Topological Memory Devices

Author

BHOWMICK, TONMOY KUMAR

Publication Date

2019

UNIVERSITY OF CALIFORNIA
RIVERSIDE

Charge Transport, Spin Transport and Magneto-Optics of Solid-State Topological Memory Devices

A Dissertation submitted in partial satisfaction
of the requirements for the degree of

Doctor of Philosophy

in

Electrical Engineering

by

Tonmoy Kumar Bhowmick

March 2019

Dissertation Committee:

Dr. Roger K. Lake, Chairperson
Dr. Ran Cheng
Dr. Nathaniel M. Gabor

The Dissertation of Tonmoy Kumar Bhowmick is approved:

Committee Chairperson

University of California, Riverside

Acknowledgments

I am grateful to my supervisor Prof. Roger K. Lake for his continuous guidance and invertible suggestion throughout the research. I am also grateful to my lab-mates, especially Dr. K. M. Masum Habib, Dr. Darshana Wickramaratne, Dr. Yafis Barlas and Dr. Mahesh Neupane for their help in my research projects. My utmost gratitude goes to my collaborators including Dr. Jiadong Zang, Dr. Amrit De for their important contributions to my research projects and kind guidance for my career. Special thanks to my friends for their company and support.

The text of this dissertation, in part or in full, is a reprint of the material as it appears in the following journals and/or proceedings:

- Physical Review B [1]. Reprinted with permission from [1]. [2018] American Physical Society (APS).

The co-author Roger K. Lake, listed in the above publications directed and supervised the research which forms the basis for this dissertation. The remaining co-authors listed provided technical expertise and support as collaborators. This work was supported by the NSF ECCS-1408168 Physical Mechanisms and Limits of Skyrmions for Information Processing and Storage and as part of the Spins and Heat in Nanoscale Electronic Systems (SHINES) an Energy Frontier Research Center funded by the U.S. Department of Energy, Office of Science, Basic Energy Sciences under Award #DE-SC0012670.

To my parents for all the support.

ABSTRACT OF THE DISSERTATION

Charge Transport, Spin Transport and Magneto-Optics of Solid-State Topological Memory Devices

by

Tonmoy Kumar Bhowmick

Doctor of Philosophy, Graduate Program in Electrical Engineering
University of California, Riverside, March 2019
Dr. Roger K. Lake, Chairperson

Topological spin textures such as skyrmions are strong candidates for next-generation storage units and spintronic devices. Skyrmions formed on the surface of topological insulators (TIs) give rise to additional device functionalities. The skyrmion-TI heterostructure system shows quantized topological Hall effect (QTHE) without any external magnetic field. This shows that the topological properties of the skyrmion spin texture can be imprinted on the Dirac electrons of the topological insulator. We also predict such a skyrmion-TI heterostructure will give rise to high figure-of-merit magneto-optic Kerr effects (MOKE). Optical dielectric tensor elements are calculated using a tight-binding model and the Kubo formula. We show that the Fermi level dependence of the MOKE signatures is distinct for the different magnetic textures. Based on this, a skyrmion optical memory device is proposed. Next, we investigate antiferromagnetic (AFM) skyrmion since it offers couple of advantages in terms of speed and stability compared to its ferromagnetic counterpart. We investigate how AFM skyrmions can be manipulated using temperature gradient to realize novel spintronic device. The effect of temperature gradients on AFM skyrmion dynam-

ics is predicted using a numerical Landau Lifshitz Gilbert (LLG) model. Finally we also demonstrate an AFM-TI heterostructure will also give rise to high figure-of-merit MOKE signal.

Contents

List of Figures

List of Tables

Chapter 1

Introduction

For the past few decades, topologically non-trivial phenomena has been at the forefront of the solid state physics research community [2]. The study of quantum Hall effect in the early 1980's revealed a new topological order in the quantum Hall states which resulted in integer Hall conductance in such a system [3–8]. Quantum Hall effects have been studied in two dimensional electron gases found at the interface of different material systems. These effects can be explained from the single-particle physics of kinetic energy quantization and Landau level formation in a two-dimensional system where Landau level energy gaps occur only at integer values of the Landau level filling factor. The demonstration of perfectly quantized conductivity in a highly disordered system opened up a new horizon for modern solid state physics.

After the discovery of topological order in the solid state, physicists realized a new quantity is needed to describe the topological order in the quantum anomalous Hall (QAH) state [6, 7, 9, 10]. This quantity is described as the Chern number, which represents the integer counts how many times the directional solid angle of k-space Bloch states wrap a unit sphere in Hilbert space. In a topologically ordered phase, physical response function is given by a Chern number. Chern numbers describe a topological phase which is insulating but always has metallic edges/surfaces when put next to the vacuum or an ordinary phase.

The real space topological order can be described by a skyrmion where the analogue of Chern number means how many times the spins of a skyrmion wraps the Bloch sphere [11, 12]. This real-space spin homotopy is equivalent to rotation in an unit sphere in spin space, which introduces an integer topological charge for each skyrmion [13, 14]. Due to this topological order, each skyrmion possesses a unit magnetic flux quantum, that demonstrates itself in the form of a quantized topological Hall effect, which arises from non-trivial Berry phase in momentum space [15]. This leads to a geometric topological Hall (TH) effect, which has been experimentally demonstrated in skyrmion hosting materials. Their stabilization and dynamics of individual skyrmions depend strongly on their topological properties which makes skyrmions an ideal candidate for topological spintronics [16,17]. It has been shown recently that a skyrmion network embedded in magnetic films may provide a suitable physical implementation for reservoir computing applications. Due to these exotic properties of skyrmions, storing and retrieving data using skyrmions has been a key research topic in spintronics for the last decade, and it is the focus of Chapters 1, 2, 3 and 4 in this dissertation.

In Chapter 5, we discuss magneto optic effects of a TI-AFM heterostructure which is the optical analogue of an electrical quantum anomalous Hall effect. Although the Kerr effect has been known for over a century, it has become the subject of intense investigations in the last decade due to the potential realization of modern high-density data-storage. Exchange splitting of energy bands caused by magnetization together with spin-orbit coupling (SOC) has been demonstrated as the origin of the MOKE signal. Therefore, MOKE has been explored extensively in various materials with net magnetization including ferrimagnets. In Chapter 5, we present a comprehensive first-principles study of MOKE in a TI-AFM system where it is shown here that large Kerr rotations can be obtained when two materials are combined. This is attributed to the antiferromagnet inducing an asymmetry on the two surfaces of the topological insulator that is observable in a polar Kerr effect configuration.

Chapter 2

Theory

Prior to exploring the transport properties of topological insulating materials like Bi_2Se_3 in proximity with skyrmion, a basic understanding of the underlying physics of both topological insulators and skyrmions is mandatory. Here, a brief introduction of topological insulators and skyrmions will be provided.

2.1 Topological Insulator

Edwin Hall's experiment in 1878 attempted to explain the effect of a magnetic field on the conduction properties of a metal with the help of the Lorentz force. After over a century later, Klaus Von Klitzing in 1986 explored the effect of a perpendicular magnetic field on the resistance of a quasi 2D electron gas (2DEG) which ultimately led to the Nobel Prize in 1985. His study led to the well known phenomena of the Quantum Hall Effect (QHE), which is characterized by quantized hall resistance that is basically the ratio of two fundamental constants.

The topological index for an insulator can be understood from the Berry curvature. The Berry curvature and the Chern number are two defining terms for a topological insulator. For any sample material, we can use Bloch waves to define the curvature of the bands in the two dimensional Brillouin Zone. For Bloch waves [18–20],

$$\psi_{n,\boldsymbol{k}}(\boldsymbol{r}) = u_{n,\boldsymbol{k}}(\boldsymbol{r}) exp(i\boldsymbol{k}.\boldsymbol{r}) \tag{2.1}$$

So the Berry curvature for Band n at momentum point $\boldsymbol{k}$ can be defined as

$$F_n(\boldsymbol{k}) = \int\int_{\text{unit cell}} [\nabla_{\boldsymbol{k}} u_{n,\boldsymbol{k}}(\boldsymbol{r})]^* \times \nabla_{\boldsymbol{k}} u_{n,\boldsymbol{k}}(\boldsymbol{r}) d\boldsymbol{r} \tag{2.2}$$

or the equation can be expressed as

$$F_n(\boldsymbol{k}) = -i\epsilon_{ij} \langle \partial_{\boldsymbol{k}_i} u_{n,\boldsymbol{k}} | \partial_{\boldsymbol{k}_j} u_{n,\boldsymbol{k}} \rangle \tag{2.3}$$

The ϵ_{ij} here is the Levi-civita symbol where $\epsilon_{xx} = \epsilon_{yy} = 0$ and $\epsilon_{xy} = -\epsilon_{yx} = 1$. The total Berry curvature calculated over the the filled bands should give us a topological index which in this case is known as the Chern number [21, 22].

$$C_n = \frac{1}{4\pi} \oint_{BZ} F_n(\boldsymbol{k}) d\boldsymbol{k} \tag{2.4}$$

For each filled band, one can get a topological index (Chern number) calculated in this manner. For an insulator, the total Chern number can be defined as

$$C = \sum_{\text{i = filled bands}} C_i. \tag{2.5}$$

The total Chern number equals the total number of the chiral edge states. When an insulator has a non-zero Chern number, it becomes the topological insulator or Chern insulator and such a topological insulator has a total number of chiral edge states equal to the Chern number for that insulator. The longitudinal conductivity σ_{xx} becomes zero and the Hall conductivity is $\sigma_{xy} = \frac{Ce^2}{h}$ [23].

σ_{xy} is stable against impurities in a topological insulator mainly due to the fact that even if the topological insulator system is perturbed, the perturbation will not change the topology of the system, so the value of the Hall conductivity σ_{xy} will be constant. Topological insulating properties of material were first demonstrated in the HgTe/CdTe quantum well heterostructues. Since then topological insulating properties have been discovered in new kinds of 3D material like $\mathrm{Bi}_{1-x}\mathrm{Sb}_x$ (the first 3D topological insulator), $\mathrm{Bi_2Se_3}$, $\mathrm{Bi_2Te_3}$, $\mathrm{Sb_2Te_3}$ (the second generation of topological insulator) [24, 25].

2.2 Skyrmion

Around 1961, nuclear physicist Tony H. Skyrme proposed the idea that the inner portion of a nucleus may be thought of as a medium formed from a three pion field [26]. Skyrmions according to his model are smooth, topologically stable field configuration where the field configuration vanishes at spatially infinite distance and has a finite energy. Within the general theoretical framework of Tony Skyrme's model, skyrmions have recently gained attention in condensed matter physics, micro-magnetics and other more applied fields of science mostly due to the unique topological attributes of the skyrmions and the ease at which researchers around the world have been able to manipulate them. Skyrmions can be found in both bulk-materials and two dimensional systems [15, 27]. From the topological perspective, skyrmions are similar to magnetic bubbles which were extensively explored in the 1970-1980's due to the rapid technological growth predicted by Moore's law and in search for devices to store data with higher data density [28]. Skyrmions are non-collinear spin textures that can be characterized by a topological number [29]

$$N = \frac{1}{4\pi} \int \boldsymbol{n} \cdot (\frac{\partial \boldsymbol{n}}{\partial x} \times \frac{\partial \boldsymbol{n}}{\partial y}) dA. \tag{2.6}$$

The origin of the skyrmion can be mostly attributed to the Dzyaloshinskii-Moriya interaction (DMI) [30–34]. The key ingredient for a material to exhibit magnetic properties is the symmetric exchange interaction, as a result of which the neighboring magnetic moments of the unit cell or atoms want to point in the same or opposite direction depending on the sign of the exchange interaction term (positive or negative) to minimize the ground state energy of the entire system. In mathematical terms, the exchange interaction term can be written as

$$H = -J \sum_{<i,j>} \boldsymbol{s}_i . \boldsymbol{s}_j \tag{2.7}$$

This energy is smallest (largest) if $\boldsymbol{s}_i$ and $\boldsymbol{s}_j$ point in the same (opposite) direction for a positive value of J.

Another kind of magnetic interaction that arises from the lack of inversion symmetry is the Dzyaloshinskii-Moriya Interaction (DMI) which is also known as asymmetric exchange. The DM interaction in the first order approximation can be expressed as $H_D = \boldsymbol{D}_{ij} . (\boldsymbol{s}_i \times \boldsymbol{s}_j)$ where the term $\boldsymbol{D}_{ij}$ is a material dependent constant. When the DM interaction term is included in the Hamiltonian in Eq. (2.7), the system energy reduces if the angle between the spin $\boldsymbol{s}_i$ and $\boldsymbol{s}_j$ is 90^0 and the angle is oriented so that the crossproduct develops a negative sign. The DMI term tries to align the spins $\boldsymbol{s}_i$ and $\boldsymbol{s}_j$ so that the plane containing the vectors is perpendicular to the DMI vector $\boldsymbol{D}_{ij}$.

When the ferromagnetic exchange and DM interaction both are present in the system, the competition between these two forces tries to drive the material into different areas of the phase space. When these two forces are present simultaneously, the configuration that minimizes the energy is neither perfectly parallel (anti-parallel) or perpendicular but a helix or chiral state. The properties of the helix depends on the ratio of D/J.

2.2.1 Skyrmion Material

Since the first discovery of skyrmions in MnSi [35], skyrmions have been explored in a number of materials, each unique for its unique characteristics. All of these skyrmion materials are known as the B20 compounds which have the space group $P2_13$ with cubic Bravais lattice structure [36]. Only 12 symmetry operations can be done on this space group which makes it the smallest one compatible with the cubic lattice among the Bravais lattices . The point symmetry among the component site is C_3. Here, a short description of the most renowned skyrmion materials will be given.

Cu_2OSeO_3 is the first multiferroic material where skyrmions have been demonstrated, which, in turn, induces electric polarization. It makes Cu_2OSeO_3 an interesting candidate for further exploration where electric field control of magnetic spin chirality might be possible via magneto-electric responses. From an engineering viewpoint, manipulation of skyrmions in this type of insulating material might be particularly significant since in an insulating material the Joule heating will be negligible compared to other conducting mediums where the skyrmions are mostly manipulated by current driven dynamics.

Muenzer et al. first in 2010 investigaed the magnetic phase diagram of $\mathrm{Fe}_{1-x}\mathrm{Co}_x\mathrm{Si}$ using small angle neutron scattering [37]. In contrast to MnSi where the crystal structure and DM interaction have the same chirality, they are of opposite type in $\mathrm{Fe}_{1-x}\mathrm{Co}_x\mathrm{Si}$. Like MnSi, FeGe is a helimagnet which crystallizes in tetrahedral $P2_13$ structure like the other B20 compounds. Small angle neutron scattering reveals that the direction of the helical-q vector depends on the temperature T: below 280 K it points along the [001] direction and changes to [111] as the temperature is lowered [38]. Around 260K, the crystal structure of FeGe changes to a hexagonal skyrmion lattice making it the first material which shows the magnetic vortex phase near room termperature.

2.2.2 Experimental observaton of skyrmion

Small angle neutron scattering (SANS) which mainly utilizes the elastic scattering of neutrons at small angles to investigate magnetic order was the first experimental technique used to prove the existence of a skyrmion lattice as a bulk phase in the chiral magnet MnSi. Neutron scattering has been used for a long time to study the magnetic phase due to the fact that neutrons scatter from the magnetic structure in a solid state system due to their magnetic moment and the lack of an electric charge permits neutrons to penetrate deep into the system under investigation. During an experiment, typically a beam of neutrons is directed upon a sample, which mainly is a powder or a crystal and the neutrons scatter elastically since they posses a magnetic moment themselves which interact with the spin of the material and gets back-scattered on a screen behind the sample. A fourier analysis of the pattern recorded on the screen gives information about the topology of the magnetic structure.

In recent years, more powerful real space imaging techniques have been developed to directly visualize the spatial magnetization configuration. Some of the most prominent and widely used techniques are Magnetic Force Microscopy (MFM) and Lorentz Transmission Electron Microscopy (LTEM). Magnetic Force Microscopy (MFM) which has been derived from Atomic Force Microscopy mainly differs with MFM in the sense that whereas the Atomic Force Microscopy cantilever tip does not have a ferromagnetic sensor, the magnetic stray field from a cantilever tip coated with ferromagnetic film is present in the case of MFM. Lorentz transmission electron microscopy (LTEM) is mainly derived from traditional electron microscopy where Lorentz forces between an electron beam interacting with a magnetic sample is utilized to allow for the visualization of the magnetic structure of the material. LTEM is complementary to MFM because LTEM can not accurately specify the direction of the magnetization normal to the surface.

Chapter 3

High Figure of Merit Magneto Optics from Interfacial Skyrmions on Topological Insulators

Magneto-optic (MO) phenomenon such as Kerr and Faraday rotations, Voigt effect, magneto-plasma reflections and cyclotron resonances arise from broken time reversal symmetry. Some MO effects also arise from the electronic structure's topology, and hence are used to study quantum hall effects [39], Kerr rotations in topological insulators (TIs) [40,41], magneto-electric optical effects [42,43], magneto-chiral effects [44], and skyrmions and their Hall effects [45–47].

The magneto optic Kerr effect (MOKE) in the polar configuration is particularly interesting due to its application in optical reading–out of magnetically stored information [5–7]. A MOKE device can be characterized by its figure-of-merit (FOM) [48–50], which usually depends on the Kerr rotation angle and the reflectivity. Typically, during the MO memory write process, a focussed laser heats the magnetic material to its Curie temperature, which allows the local magnetic polarization to be flipped. However, the thermally–assisted write processes can be relatively slow. For readout, the Kerr rotation is barely one degree for most MO recording materials [51–54], which can result in higher readout error rates. The Kerr rotation can be enhanced by the use of cavity like resonance conditions, but this usually lowers the reflectivity and makes the memory write process difficult.

The required magnetic fields and effective cyclotron frequencies for generating large Kerr rotations in a semi-infinite medium can be unreasonably large [55, 56]. However, skyrmions can give rise to very high emergent fields. The emergent magnetic fields from a periodic lattice of skyrmions (SkX) can reach up to 4000 Tesla, which is two orders of magnitude larger than what can be generated in laboratories.

Skyrmions are topological particle-like configurations of continuous vector fields and are regarded as analogs of magnetic monopoles as each skyrmion is associated with a quantized magnetic flux [57, 58]. Their non-trivial topology is a result of competing Dzyaloshinkii-Moriya-(DM), Heisenberg- and Zeeman-interactions [47, 59, 60]. In addition, skyrmions represent a new type of magnetic order [11, 13], and they have been observed in B20 compounds such as MnSi [61, 62], FeCoSi [63], FeGe [64] and in Cu_2OSeO_3 which is a multiferroic [65].

The use of magnetic [66] and electric fields [67] has been proposed to switch between the topologically nontrivial skyrmion spin texture and the topologically trivial ferromagnetic spin texture. Experimentally it is possible create and erase individual skyrmions

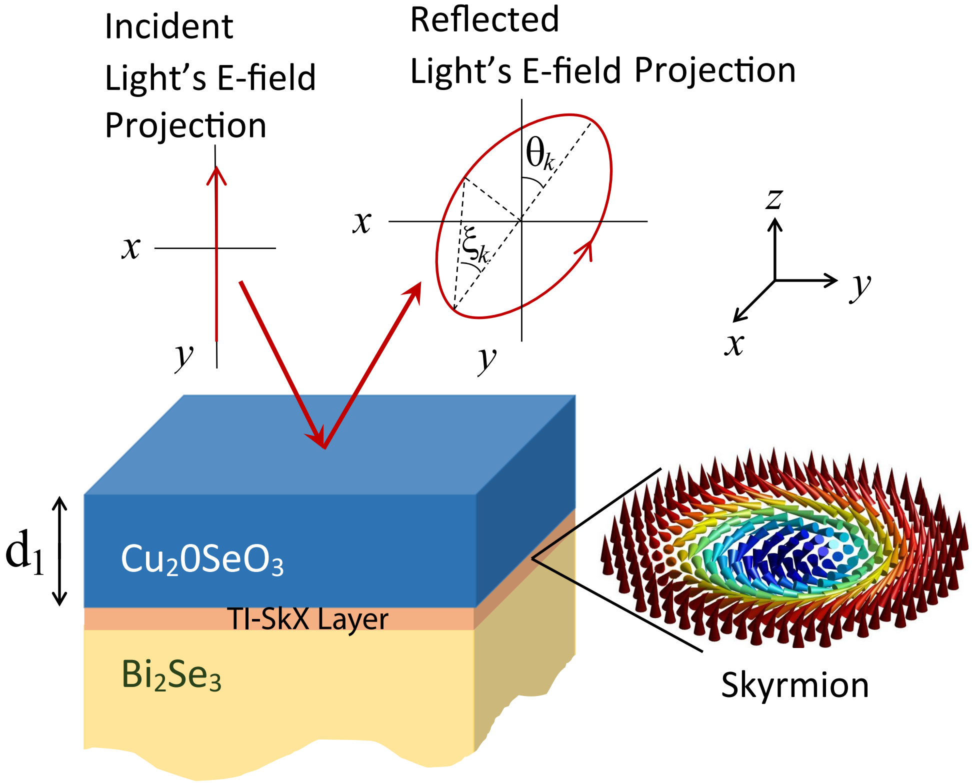

Figure 3.1: MOKE arising from a magneto-optic device with a thin-film B20 material deposited on top of a semi-infinite TI. A SkX exists at the interface of the TI and B20 compound.

using spin polarized currents [68]. Also magnetic skyrmions can be electrically created on a thin-film of a chiral-lattice magnetic insulator within a few nanoseconds by applying an electric field which couples to the noncollinear skyrmion spins [69–75]. In Cu_2OSeO_3, the noncollinear skyrmion spin structure in the host material behaves like a multiferroic due to spin orbit coupling. This enables skyrmion manipulaton via electric fields instead of electric currents [76,77] or heat pulses [78]. More recently it has been shown that one can reversibly switch between topologically inequivalent ferromagnetic phases and skyrmion phases using electric fields [79]. A topological charge analysis of skyrmion dynamics, energetics, creation, and stability was recently described [80].

Skyrmions combined with other topological materials can lead to emergent functionalities. In this paper, we show that a skyrmion lattice at the interface of a thin-film B20 compound (such as Cu_2OSeO_3) and a semiinfinite TI (e.g. Bi_2Se_3) gives rise to a high FOM-MOKE (see Fig. 6.6). The large MOKE can be exploited for characterization of the spin texture, or application in a magneto–optic memory device.

Skyrmions can form on a TI's surface [81] and can become charged [82]. The B20–TI heterostructure provides electric field switching of the skyrmion spin texture and a large MOKE from the skyrmion phase. The large differential MOKE leads to fast and high fidelity magneto–optical bit readout. Electric field switching provides fast, low–power writing. The emergent properties of the B20–TI heterostructure provide the physical mechanisms for facile reading and writing of information bits in a topological magneto-optic memory.

For simplicity we consider a device geometry where a seminfinite TI is capped by a thin Cu_2OSeO_3 layer as shown in Fig. 3.1. We consider interfaces with a ferromagnetic

(FM) texture along with Néel- and Bloch type skyrmions. This simple geometry allows us to best highlight the main MOKE spectral features manifesting from different physical effects. These are: the low energy topological MOKE, thin-film induced enhancement of MOKE and MOKE occurring at the high energy plasma frequency.

3.1 Model and Method

We begin by constructing a model where the surface of the TI is coupled to the background spin texture of a SkX. A low energy effective model describing the surface state of Bi_2Se_3 is used where the surface state consists of a single Dirac cone at the Γ point [83].

We consider the low energy effective Hamiltonian [84] describing the decoupled top and bottom surface states of a TI. To avoid the well known Fermion doubling problem on discrete tight-binding lattice, we have added a $k^2\sigma_z$ term to the Hamiltonian of TI [85,86]

$$H = \hbar v_F(k_x\sigma_y - k_y\sigma_x) - \zeta\hbar v_F(k_x^2 + k_y^2)\sigma_z, \tag{3.1}$$

where the Fermi velocity v_F, is a material constant. This momentum space Hamiltonian can be transformed into the following real space tight binding Hamiltonian coupled to the Skx spin texture on a rectangular lattice

$$H = \sum_i c_i^\dagger \epsilon c_i - \sum_{<i,j>} (c_i^\dagger t c_j + h.c.) - J_H \sum_i c_i^\dagger \boldsymbol{\sigma}_i \cdot \mathbf{S}_i c_i \tag{3.2}$$

where $\boldsymbol{S}_i$ is the localized spin of the skyrmion on site i which couples to the TI through the Hund's rule coupling constant J_H. Here t is the nearest neighbor hopping along the x and y directions, $\boldsymbol{\sigma_i}$ is the spin of the itinerant electron, and ϵ is the on site potential.

Periodic boundary conditions are imposed along both the x and y directed edges of a square unit cell consisting of 9×9 lattice sites. We define two dimensionless parameters $t_1 = \hbar v_F/2a$ and $t_2 = \zeta/a$. Here, $\epsilon = 8t_1t_2\sigma_z$, $t_x = -it_1\sigma_y - 2t_1t_2\sigma_z$, $t_y = it_1\sigma_x - 2t_1t_2\sigma_z$. For our numerical simulations we choose the discretization length $a = 15$Å, $\zeta = 5$Å, $v_F = 0.5 \times 10^6$ m/s and $J_H = 40$ meV. [81] The interplay between $t_{x,y}$ and J_H dictates the anomalous Hall conductivity of the TI surface in this model.

The magnetization of a single skyrmion can be described by

$$\mathbf{n}(\mathbf{r}) = [\sin\vartheta(r)\cos\varphi(\phi), \sin\vartheta(r)\sin\varphi(\phi), \cos\vartheta(r)], \tag{3.3}$$

where $\vartheta(r = 0) = 0$, $\vartheta(0 < r < R_s) = \pi(1 - \frac{r}{R_s})$ and $\vartheta(r > R_s) = \pi$. [29] $\varphi(\phi) = m\phi + \nu$ and $\phi = \tan^{-1}[y/x]$ where the helicity of the skyrmion is defined by the phase ν. [87] In this paper, we consider both Néel type ($m = 1, \nu = 0$) and Bloch type skyrmions ($m = 1, \nu = \pi/2$). The skyrmion is centered in the unit cell, and the magnetization $\mathbf{n}(\mathbf{r})$ is evaluated at each lattice site i to obtain $\mathbf{S}_i$ in Eq. (3.2).

The z-component of $\mathbf{n}(\mathbf{r})$ acts on the electron like position dependent Dirac mass, while the in-plane components can give rise to an emergent gauge field. The total magnetic flux enclosed in a unit skyrmion cell is one flux quantum, $\Phi_0 = h/e$, independent of the skyrmion radius, R_s. [88] The effective magnetic field is $B_{\text{eff}} = -\Phi_0/(4R_s^2)$. [89]

3.2 Electronic Structure

The numerically calculated band structure and the corresponding density of states (DOS) are shown in Fig. 3.2 for the magnetic textures proximity coupled to the TI. This

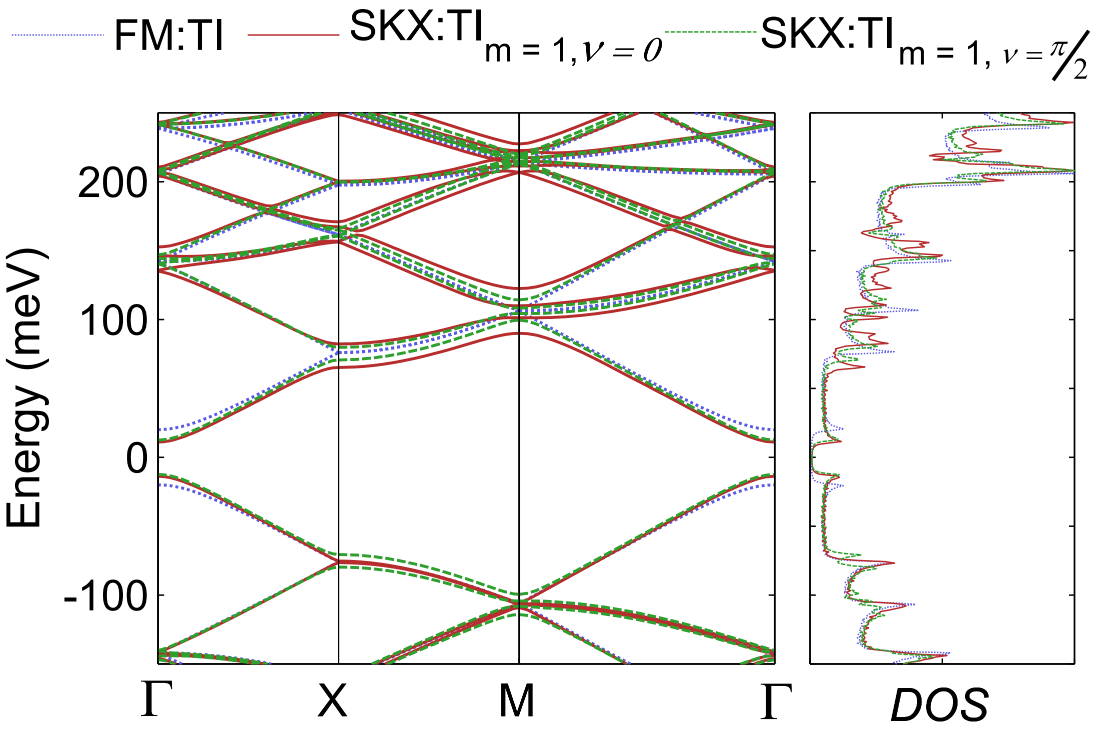

Figure 3.2: Electronic bandstructure and density of states for proximity coupled FM:TI system and SkX:TI with $m = 1$, and $\nu = 0$ and $\nu = \pi/2$

includes the ferromagnetic case (FM:TI), the Néel type skyrmion ($m = 1, \nu = 0$), and the Bloch type skyrmion ($m = 1, \nu = \pi/2$) proximity coupled to the TI's surface state. The energy gap at Γ resulting from proximity coupling to the Néel and Bloch type skyrmions is less than the gap resulting from proximity coupling to the FM state. This can be understood from the fact that the skyrmion creates a hole in the background FM texture that reduces the total $\hat{z}$ component of the magnetic moment. The presence of the skyrmions also breaks the degeneracy in other higher energy regions of the spectrum.

3.3 Dielectric Tensor Components

Observables such as magneto optic effects and quantum Hall type phenomenon manifest themselves through the dielectric tensor components which depend on the electronic structure and topological properties. In the case of normal optical incidence for an SkX on a TI, the magnetization is along z, which is perpendicular to the surface and parallel to the direction of light propagation, similar to the polar Kerr effect. The x and y directions preserve in-plane symmetry. The complex 3×3 dielectric tensor has diagonal $[\epsilon_{xx}, \epsilon_{yy}, \epsilon_{zz}]$ terms and the off-diagonal ϵ_{xy} terms which are topology dependent.

The matrix elements of the optical conductivity tensor can be obtained from the band structure calculations using the Kubo formula [2, 90] as follows:

$$\sigma_{\imath\jmath} = \frac{ie^2}{(2\pi L)^2 \hbar} \int \frac{d\boldsymbol{k}}{2\pi} \sum_{n,l} \frac{f_{nl}(\boldsymbol{k})}{\omega_{nl}(\boldsymbol{k})} \left(\frac{\Pi(\boldsymbol{k})^{\imath}_{nl} \Pi(\boldsymbol{k})^{\jmath}_{ln}}{\omega_{nl}(\boldsymbol{k}) - \omega + i\gamma} + \frac{\Pi(\boldsymbol{k})^{\imath}_{ln} \Pi(\boldsymbol{k})^{\jmath}_{nl}}{\omega_{nl}(\boldsymbol{k}) + \omega + i\gamma} \right) \tag{3.4}$$

where $\Pi^{\imath}_{nl}(\boldsymbol{k}) = \langle \psi_n(\boldsymbol{k}) | v_{\imath} | \psi_l(\boldsymbol{k}) \rangle$ is the velocity operator. Here $\{\imath, \jmath\} \in \{x, y\}$, γ is a broadening parameter and $\hbar\omega_{nl}(\boldsymbol{k}) = E_n(\boldsymbol{k}) - E_l(\boldsymbol{k})$, is the energy difference of an optical transition between an unoccupied band, n and an occupied band, l. $f_{nl}(\boldsymbol{k}) = f_n(\boldsymbol{k}) - f_l(\boldsymbol{k})$, where $f_n(\boldsymbol{k})$ is the Fermi filling factor. Since we are using an effective Hamiltonian to obtain $\sigma_{\imath\jmath}$, we compensate for the missing higher band contributions in Eq. (6.3) by adding a $\kappa/(\omega+i\gamma)$ term while relating the optical dielectric tensor to the conductivity tensor.

$$\epsilon_{\imath\jmath}(\omega) = \varepsilon_o \delta_{\imath\jmath} - \frac{4\pi i}{\omega}\sigma_{\imath\jmath} - \frac{\kappa}{\omega + i\gamma} \tag{3.5}$$

Here κ is adjusted so that the relative zero frequency dielectric constant ϵ_0 matches the known experimental value. ε_o is the vacuum permittivity. For $\mathrm{Bi_2Se_3}$, $\epsilon(\omega)$ is given by Lorentz oscillator fits to experiment [91], which in the low energy regime ($0 - 30$ meV) is essentially a constant. In the effective surface model, the bulk band contributions to the momentum matrix elements in $\epsilon_{\imath\imath}(\omega)$ are not included. However, this does not change the qualitative behavior of the effects shown in this paper, since the calculated $\epsilon_{\imath\imath}(\omega)$s are qualitatively similar to experiment [91]. Therefore we argue that all the higher energy MOKE features disccused in this paper would still be seen in experiments, but at higher optical frequencies.

The dielectric function consists of Berry connection type terms, $a_\imath(\boldsymbol{k})$, which behave like a fictitious momentum space gauge potential or an equivalent magnetic field $b_z(\boldsymbol{k}) = \partial_{k_x} a_y(\boldsymbol{k}) - \partial_{k_y} a_x(\boldsymbol{k})$. The MOKE can therefore be viewed as an optical manifestation of the Berry curvature via the ϵ_{xy} term. This is similar to charge transport, where the xy response is proportional to the Chern number [13, 92–94], which is the integral of Berry curvature over the first Brillouin zone, $\mathcal{C} = \frac{1}{2\pi}\int d^2k b_z(\boldsymbol{k})$. There are differences between MOKE and quantum Hall effect type topological manifestations due to conduction ↔ valance transitions and the frequency dependence in optics. ϵ_{xy} depends on the topological charge across a gap. Usually ϵ_{xy} is much smaller than the diagonal ϵ_{xx}. In our case the three different magnetic textures result in the same Chern number across the fundamental gap of the proximity induced magnetic TI surface state, so that ϵ_{xy} does not vary much when the Fermi energy is set to 0.

3.4 Magneto-Optics

The complex in-plane index of refraction is $n_\pm = \sqrt{\epsilon_\pm} = \sqrt{\epsilon_{xx} \pm i\epsilon_{xy}}$ where, the $+(-)$ signs represents right(left) circularly polarized (RCP(LCP)) light propagation. The complex MOKE effect is expressed as: $\Theta_k = \theta_k + i\xi_k$ where the Kerr rotation and ellipticity are, respectively

$$\theta_k = (\Delta_+ - \Delta_-)/2 \tag{3.6}$$

$$\xi_k = (|r_+| - |r_-|)/(|r_+| + |r_-|). \tag{3.7}$$

Since the eigen-modes here are LCP and RCP, the Kerr rotation angle can be expressed as the phase difference between these two modes. The complex phase $\Delta_\pm$ can be obtained from the Fresnel reflection coefficients $r_\pm$.

The MOKE arising because of the thin-film structure can be significantly altered by internal reflection at various interfaces of the layers. A 2 × 2 characteristic matrix method can be used to characterize the MOKE spectra of a multilayer structure at normal incidence, assuming that the materials are homogeneous and isotropic. The transfer matrices are in the LCP/RCP eigenmode basis, which for N parallel layers is:

$$\boldsymbol{S}^\pm = \prod_{j=0}^{N} \frac{1}{t^\pm_{j,j+1}} \begin{bmatrix} 1 & r^\pm_{j,j+1} \\ r^\pm_{j,j+1} & 1 \end{bmatrix} \begin{bmatrix} e^{i\beta^\pm_{j+1}} & 0 \\ 0 & e^{-i\beta^\pm_{j+1}} \end{bmatrix} \tag{8}$$

The Fresnel reflection and transmission coefficients at normal incidence for each interface are respectively given by: $r^{\pm}_{j,j+1} = (n^{\pm}_{j} - n^{\pm}_{j+1})/(n^{\pm}_{j} + n^{\pm}_{j+1})$ and $t^{\pm}_{j,j+1} = (2n^{\pm}_{j})/(n^{\pm}_{j} + n^{\pm}_{j+1})$ The phase factor is given by $\beta_j = (2\pi/\lambda)n_j d_j$, where d_j is the thickness of the j^{th} layer and λ is the optical wavelength. The complex reflection coefficient from the resultant characteristic transfer matrix is: $r^{\pm} = S^{\pm}_{12}/S^{\pm}_{11} = |r^{\pm}| \exp(-i\Delta_{\pm})$ where $S^{\pm}_{\imath\jmath} \in \boldsymbol{S}^{\pm}$. The observed reflective intensity is $R_{\pm} = |r_{\pm}|^2$.

3.5 Discussion

We first consider only an ideal single interface for our initial analysis. The MOKE spectra and reflectivity and the optical dielectric function are shown for a Néel type skyrmion ($m = 1, \nu = 0$) on a TI in Fig. 3.3 for illustration. The corresponding spectra for FM:TI and Bloch type skyrmion ($m = 1, \nu = \pi/2$) on a TI look very similar.

Two distinct resonance like features can be seen for the Kerr rotation and the elipticity. From the approximation [95]: $\Theta_k \approx [n_+ - n_-]/[n_+ n_- - 1]$, it is easy to see that MOKE resonances spectrally occurs whenever $\epsilon_+\epsilon_- \sim 1$ [55]. In Fig. 3.3, one MOKE resonance is in the low energy regime and occurs at 38 meV. This is close to the size of the fundamental gap that the magnetic texture (Néel type skyrmion in this case) induces in the TI. We will explore this regime, where the quantization effects occurs, in more detail later in this paper.

The high energy MOKE resonance features occur in the energy regime where free electron like behavior dominates. Hence this can be qualitatively understood from the semiclassical Drude model: $\epsilon_{\pm} \propto \left(1 - \omega_p^2/[\omega(\omega \pm \omega_c + i\gamma)]\right)$, where ω_p is the plasma frequency and ω_c is the cyclotron frequency. If $\epsilon_{xy} \ll \epsilon_{xx}$ [95], an additional approximation can be made for the Kerr rotation, $\Theta_k \approx \epsilon_{xy}/(1-\epsilon_{xx})\sqrt{\epsilon_{xx}}$. From this most commonly used expression for calculating MOKE, it can be seen that MOKE resonances should occur when $\epsilon_{xx} = 1$. This is also where $R_\pm$ goes to zero and the MOKE resonance occurs near $\omega = \omega_p$ [96–98]. Note that similarly, magneto-plasmons in graphene give large magneto optic effects [3, 4]. Using the Drude model, one can derive a simple expression for the spectral occurrence of this MOKE resonance [55]

$$\omega_\pm \approx \frac{1}{2}\left(\gamma + \sqrt{\omega_c^2 - \gamma^2 + 4\omega_p^2} \pm \omega_c\right) \tag{3.8}$$

In an attempt to explain the high energy spectral features using the Drude model, we extract the effective ω_p and effective ω_c using the optical sum rules:

$$\int_0^\infty \omega Im[\epsilon_{xx}(\omega)]d\omega = \frac{\pi}{2}\omega_p^2 \tag{3.9}$$

$$\int_0^\infty \omega^2 Re[\epsilon_{xy}(\omega)]d\omega = -\frac{\pi}{2}\omega_p^2\omega_c \tag{3.10}$$

These values can be substituted into Eq. (3.8) to obtain ω_+, which is listed in Table 3.1 along with other parameters. The analytically obtained ω_+ is in excellent agreement with ω_θ – which is the frequency at which the high energy MOKE resonance occurs. In this high energy regime, the magnitude of $\theta_k^{max} \propto \omega_c\omega_p^2 \propto \epsilon_{xy}$ as shown in Table 3.1. Note that these calculations are for a single interface (i.e. assuming both the Cu_2OSeO_3 and Bi_2Se_3 layers are semi-infinite).

We next consider the MOKE features around 38 meV. The MOKE spectra is shown in Fig. 3.4 in the energy regime below 300 meV. The maximum Kerr rotation is about 9°, which occurs when $R_\pm$ are the furthest apart as this increases $\Delta_+ - \Delta_-$. The Kerr rotation

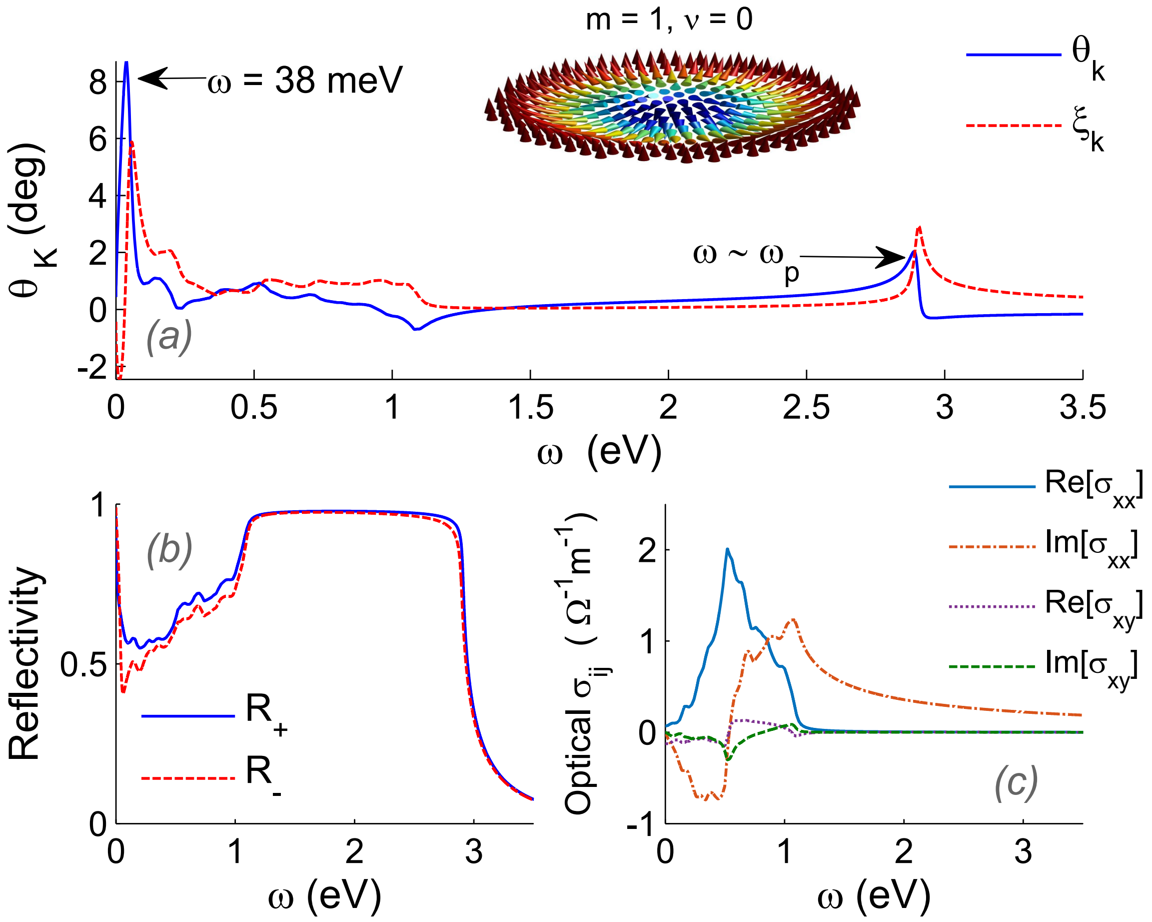

Figure 3.3: (a) Kerr rotation and ellipticity for a single SkX:TI interface for Néel type skyrmion $m = 1, \nu = 0$ (b) Reflectivity for left- and right-circularly-polarized light. (c) The corresponding optical conductivity of SkX:TI system

Spin Texture	$\theta_k^{\omega_p}$	ω_p (eV)	ω_c (eV)	ω_θ (eV)	ω_+ (eV)
FM	2.175	2.822	0.014	2.894	2.878
$m = 1, \nu = 0$	2.032	2.816	0.013	2.888	2.872
$m = 1, \nu = \pi/2$	2.029	2.816	0.013	2.889	2.872

Table 3.1: List of high energy (> 2 eV) Kerr rotation angles and related parameters due to free electron like behavior for various magnetic textures on TI. Maximum Kerr rotation angle $\theta_k^{\omega_p}$, effective plasma frequency $\theta_k^{\omega_p}$, cyclotron frequency ω_c, frequency of maximum Kerr rotation ω_θ, and its predicted value ω_+.

is sufficiently large for magneto-optic recording applications. In this case, there is not a clear distinguishing feature between the interface with the FM and the interface with the two different skyrmion spin textures. For these calculations, the Fermi Energy, $E_f = 0$. The MOKE spectral features in this energy regime are primarily dominated by the gap in the TI surface state, which is induced by the magnetic textures. The Chern number in the gap is the same for all three magnetic textures, and hence there is no clear distinction in the MOKE features for $E_f = 0$.

MOKE can also be enhanced by the resonance like effects that arise from adjusting the film thickness of different materials. In order to understand the effects of this for our system, we consider a thin-film structure as shown in Fig. 3.1 where a Cu_2OSeO_3 film of thickness d_1 sits on a semi-infinite Bi_2Se_3 layer. The dispersion relation for Cu_2OSeO_3 was obtained using experimentally fitted Lorentz oscillators [99]. As is typical with multiferroics, there are several low energy phonon modes present in the Cu_2OSeO_3 dielectric function which are also reproduced by the model [99]. We assume that the SkX system exists in a 1 nm thin layer at the interface of the Cu_2OSeO_3 thin film and seminfinite Bi_2Se_3 layer.

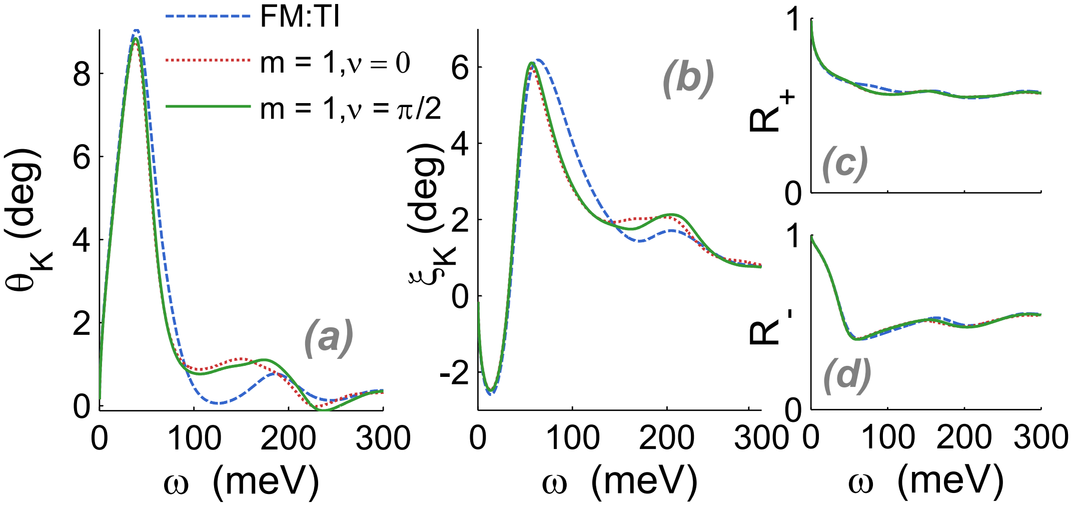

Figure 3.4: A comparison of the (a) Kerr rotation, (b) ellipticity, (c) RCP reflectivity, and (d) LCP reflectivity for FM:TI and SkX:TI with m = 1, $\nu = 0$ and m = 1, $\nu = \pi/2$.

The SkX:TI effects manifest themselves via $n_{\pm}$. The refractive index of air is used for the semi-infinite media above the Cu_2OSeO_3 layer.

A comparison of the magneto optic Kerr rotation, ellipticity, LCP and RCP reflectivity spectra are shown in Fig. 3.5 for a Néel type skyrmion, the Bloch type skyrmion, and the FM:TI for a Cu_2OSeO_3 layer with film thickness $d_1 = 200\ \mu m$. At this particular film thickness, $R_- \to 0$, which causes a huge Kerr rotation resonance of $\sim 90°$ as the phase difference between LCP and RCP is maximized. Also for a given film thicknesses for the Cu_2OSeO_3 layer, the MOKE spectra can be notably different between the different SkX textures and the FM state. In this example the maximum Kerr rotation arising from the FM:TI is $\sim$ 60 deg and occurs at a different optical frequency. In order to achieve low error magneto-optic readouts, the different states should be maximally discernable. We therefore

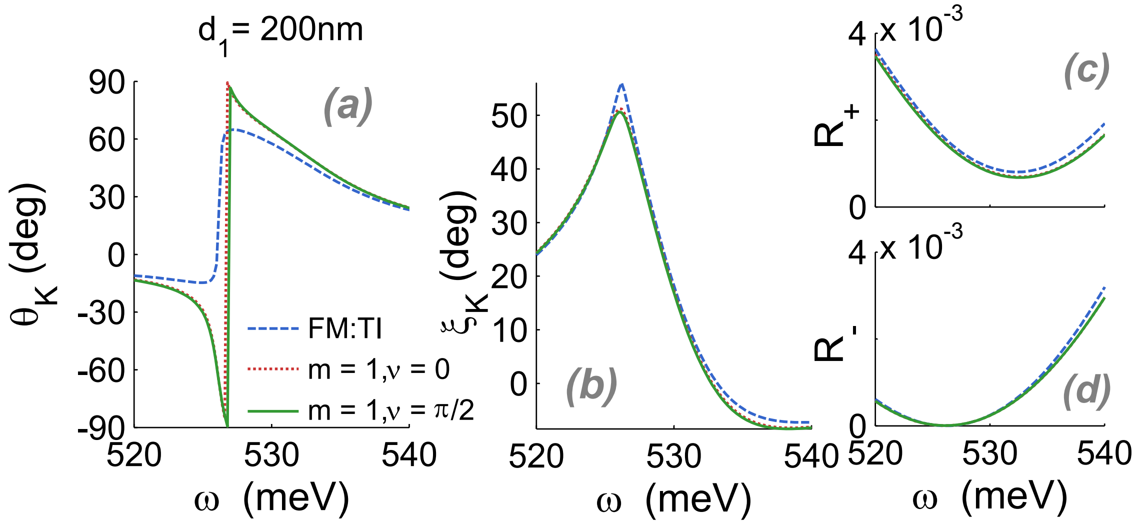

Figure 3.5: A close-up comparison of the $d_1 = 200$ nm thin-film induced resonances in the (a) Kerr rotation and (b) ellipticity. The corresponding (c) RCP reflectivity and (d) LCP reflectivity is also shown for the FM:TI- and SkX:TI interfaces with Bloch (m=1, $\nu = \pi/2$) and Néel (m=1, $\nu = 0$) type skyrmions.

examine the phase diagram, as a function of ω and d_1, for the differential MOKE effects,

$$\Delta\theta_k = \theta_k^{FM:TI} - \theta_k^{SkX:TI} \tag{3.11}$$

$$\Delta R_{av} = R_{av}^{FM:TI} - R_{av}^{SkX:TI} \tag{3.12}$$

where $R_{av} = (R_+ + R_-)/2$ is the average reflectivity. We take arctan[tan(θ_k)] to avoid Kerr rotations greater than ±90 deg.

The phase diagram for both the Kerr rotation and the average reflectivity is shown in Fig. 3.6 (a) and (c) for the Néel type skyrmion. Both Néel- and Bloch-type skyrmions have identical phase diagrams where θ_k and R_{av} vary periodically with ω and d_1. There are several periodic parts of this phase diagram that are insensitive to errors in film-thickness or spectral tuning. The reflectivity would, however, be low in this case when θ_k is maximized. The differential $\Delta\theta_k$ and ΔR_{av} effects are shown in Fig. 3.6 (b) and (d), respectively.

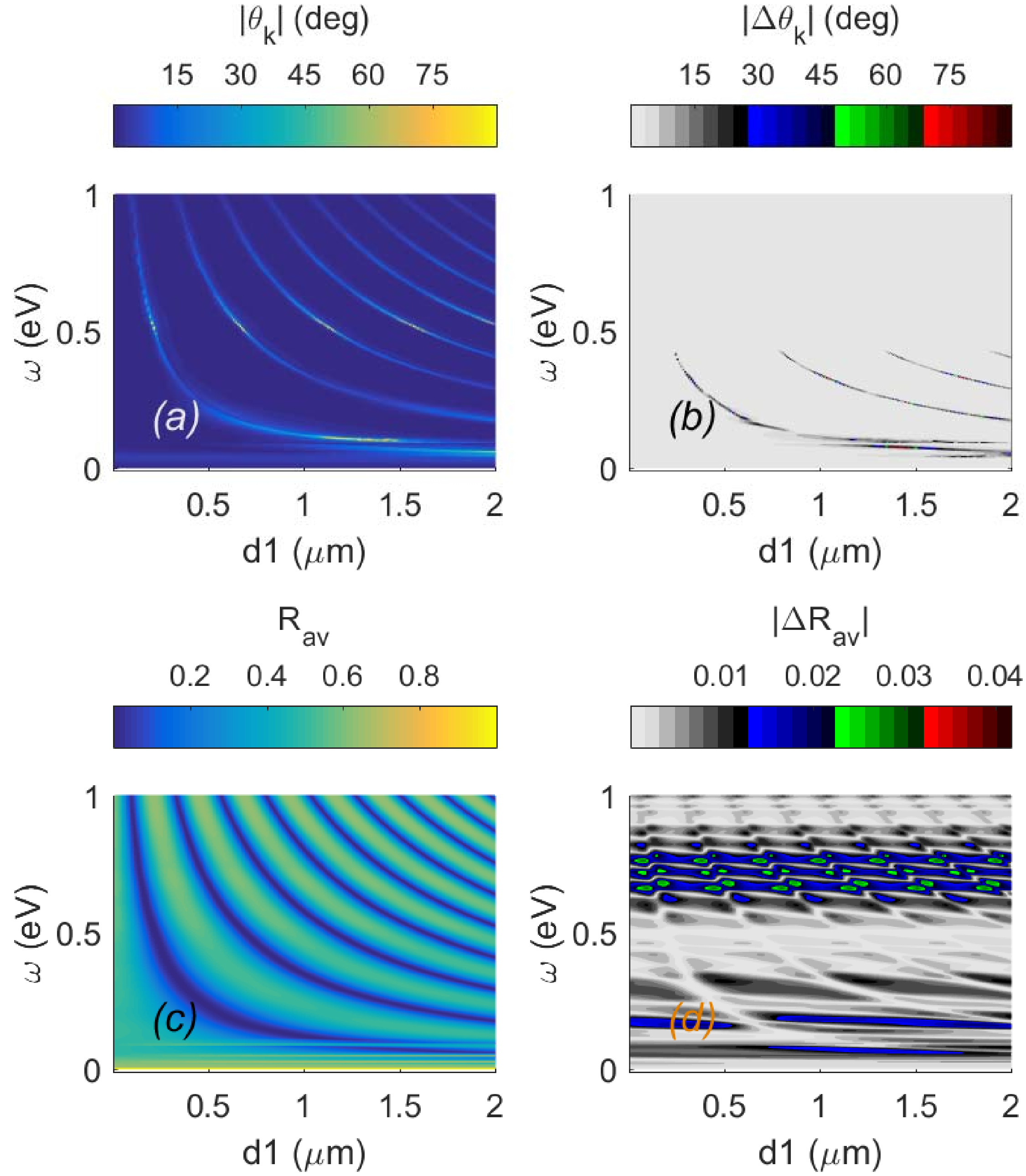

Figure 3.6: (a) The Kerr rotation for the Néel type ($m = 1,\ \nu = 0$) interface (b) and its Kerr rotation difference with the FM interface, $\Delta\theta_k = \theta_k^{FM:TI} - \theta_k^{SkX:TI}$ as a function of frequency and Cu_2OSeO_3 film thickness d_1. (c) Average reflectivity $R_{av} = (R_+ + R_-)/2$ for Néel type interface and (d) Difference in the average reflectivity: $\Delta R_{av} = R_{av}^{FM:TI} - R_{av}^{SkX:TI}$

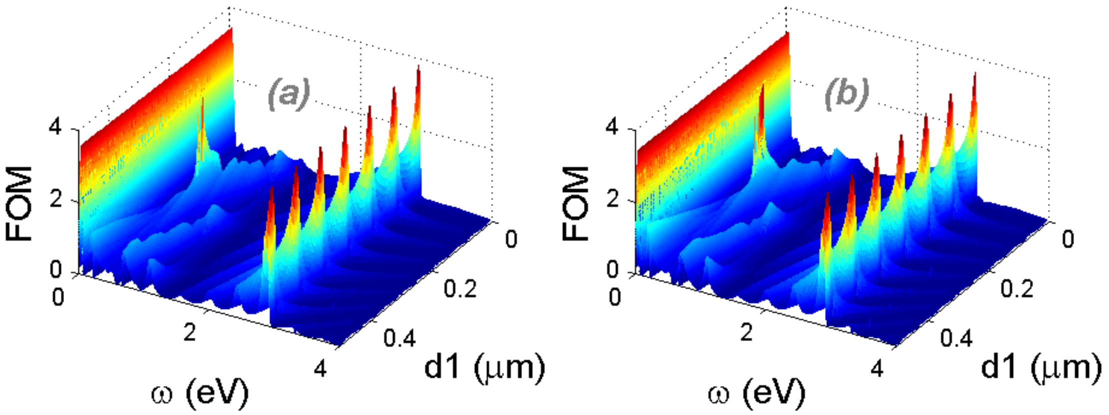

Figure 3.7: Figure of merit for (a) FM:TI (b) Néel SkX:TI

Generally ΔR_{av} is low. The FM:TI and SkX:TI have slightly different periodicity. Therefore the differential Kerr rotation can reach up to ±90° depending on d_1. The phase diagram also suggests that either the Néel- or Bloch-type skyrmions could be used for such a magneto-optic recording device.

Typically, large Kerr rotations are accompanied by low reflectivities which reduces the effectiveness of a MO device. The overall useful MO signal can be quantified by the figure of merit (FOM) [48–50] for the Kerr rotation configuration, defined here as,

$$FOM = |\theta_k| \times \max(|r_+|, |r_-|). \tag{3.13}$$

This can be used to characterize MO memory and other MO devices such as modulators and isolators.

For our device, the FOM is shown in Fig. 3.7 as a function of ω and d_1. At $\omega \approx \omega_p \approx$ 2.8 eV, the FOM peaks, arising from the free electron behavior, periodically as a function of d_1. The FOM resonance at $\omega \approx$ 0.52 eV, and $d_1 = 0.2$ μm is due to the features shown in Fig. 3.5. Even though $\theta_k \sim 90^o$, the FOM is not the highest due to low $R_\pm$. The FOM peak here is higher for the Néel SkX:TI than it is for the FM:TI. Also note that the Néel and Bloch SkX:TI's FOM are identical.

Finally, the most fascinating result is that the FOM at $\omega \approx 38$ meV is independent of d_1. This is an encouraging result for experiments and for devices as this implies that the MO-FOM is independent of any error in the Cu_2OSeO_3 film-thickness. Also, this FOM at the gap energy is also the highest in the entire FOM phase diagram.

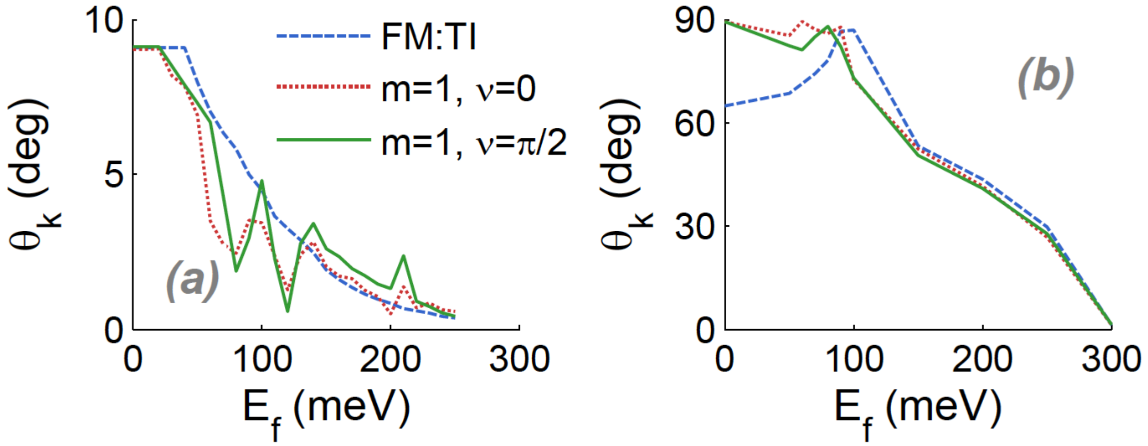

Figure 3.8: (a) Low energy spectral regime Kerr rotation, θ_k, as a function of Fermi energy, E_f, calculated around $\omega \sim 38$ meV, which is where θ_k^{max} occurs in Fig. 3.4 at $E_f = 0$. (b) Thin-film thickness ($d_1 = 200$ nm) induced Kerr rotation in the intermediate spectral regime, as a function of Fermi energy. Kerr rotations are calculated around $\omega \sim 520$ meV, which is where θ_k^{max} occurs for $E_f = 0$ in Fig. 3.5.

Finally, we study electro-optic switching effects as a function of Fermi energy. In Fig. 3.8(a), θ_k is shown as a function of Fermi energy E_f. All values are shown at the ω at which θ_k^{max} occurs for $E_f = 0$ in the low energy regime (see Fig. 3.4). Similarly Fig. 3.8(b), θ_k is shown as a function of E_f in the intermediate energy regime. Here ω for each magnetic texture is where the resonances induced by the Cu_2OSeO_3 film thickness occur in Fig. 3.5(a). In Fig. 3.8(a), all three textures show distinct behavior. While θ_k^{max} for the FM:TI shows a monotonic decrease with increasing E_f, the Néel type and Bloch type SkXs show somewhat oscillatory non-monotonic behavior. This can be explained as follows. In the present model for the FM:TI all the states above the gap are degenerate and free electron like. Hence θ_k decreases monotonically with E_f. Whereas in case of the SkX:TI, the states just above the gap are non-degenerate and the bands are split. This leads to additional peaks and valleys in the DOS, which causes the sudden jumps in Fig. 3.8(a) as E_f moves up in energy. Lastly θ_k as a function of E_f differs for the Néel type and Bloch type SkXs because their density of states is different above the gap as shown in Fig. 3.2. These effects can be numerically heightened if J_H is increased tenfold. The band-splittings in Fig. 3.2 for the two SkXs, then evolve into energy gaps where the SkXs have different Chern numbers in the gaps. This will lead to very distinct MOKE signatures as a function of E_f.

These E_f dependent non-monotonic θ_k effects are not seen in Fig. 3.8(b), where the MOKE resonances are induced by the Cu_2OSeO_3 thin-film. Here, the Néel type and Bloch type SkXs are indistinguishable, but they both differ from the FM:TI. θ_k at $E_f = 0$ is much smaller for the FM:TI because $d_1 = 200$ nm is not optimal in this case. The FM:TI and SkX:TI show distinct differences only for low E_f.

Chapter 4

Quantized Anomalous Hall Effect in Topological Insulator Coupled to Skyrmion Crystal

Since the discovery of topological insulators (TI) [100–104], exploring the properties of topological surface states in close proximity with ferromagnetism has been one of the key interests in the condensed matter physics community [105–114]. Breaking time reversal symmetry (TRS) on the surface of a topological insulator leads to novel and exciting physical effects such as the quantized anomalous Hall current [115] and the inverse spin-galvanic effect [116]. Recently, the quantized anomalous Hall effect (QAHE) has been experimentally observed on the surface of a magnetic topological insulator where the magnetization was achieved by either doping the surface of the TI [105] or coupling the surface states of the TI to a uniform magnetization through the proximity effect [117]. The effect of a real–space topological spin texture on the Dirac bands of a TI and their transport properties remains unexplored.

A magnetic skyrmion is a topologically protected real space noncollinear spin texture characterized by a topological winding number which determines how many times the spin wraps around the Bloch sphere [118–121]. Magnetic skyrmions occur in chiral magnets as a result of competition between the Dzyaloshinskii–Moriya interaction (DMI), Heisenberg exchange, and the Zeeman energy [122–124]. Skyrmions were originally discovered in MnSi [11] where lack of inversion symmetry results in a DMI. Interfacial Skyrmions at the interface between two materials with high spin-orbit coupling have also been demonstrated experimentally at room temperature where symmetry breaking at the interface leads to DMI [125].

It has been shown that an insulating skyrmion proximity coupled to a TI surface would become charged due to the localized bound states that form on the surface of the TI [82]. The existence of interfacial skyrmions on the surface of a TI has also been demonstrated experimentally for TI heterostructures composed of magnetic TI $\mathrm{Cr}_x(\mathrm{Bi}_{1-y}\mathrm{Sb}_y)_{2-x}\mathrm{Te}_3$ and non magnetic TI $(\mathrm{Bi}_{1-y}\mathrm{Sb}_y)_2\mathrm{Te}_3$ [81]. For such a system, broken spatial inversion symmetry leads to interfacial DMI which causes interfacial skyrmion formation and Rashba splitting of the bulk bands. Rashba splitting of the bulk bands leads to the sign reversal of the anomalous Hall effect, and its origin is attributed to the formation of interfacial skyrmions induced by the DMI.

How the magnitude of the proximity coupling between the TI and the skyrmion affects the QAHE and the overall phase diagram remains unknown. To answer this question, we theoretically analyze the emergence of the QAHE in a TI proximity coupled to a skyrmion. Several well separated topological electronic gaps characterized by finite integer Chern numbers appear in the continuous Dirac bands of the TI in the presence of SkX.

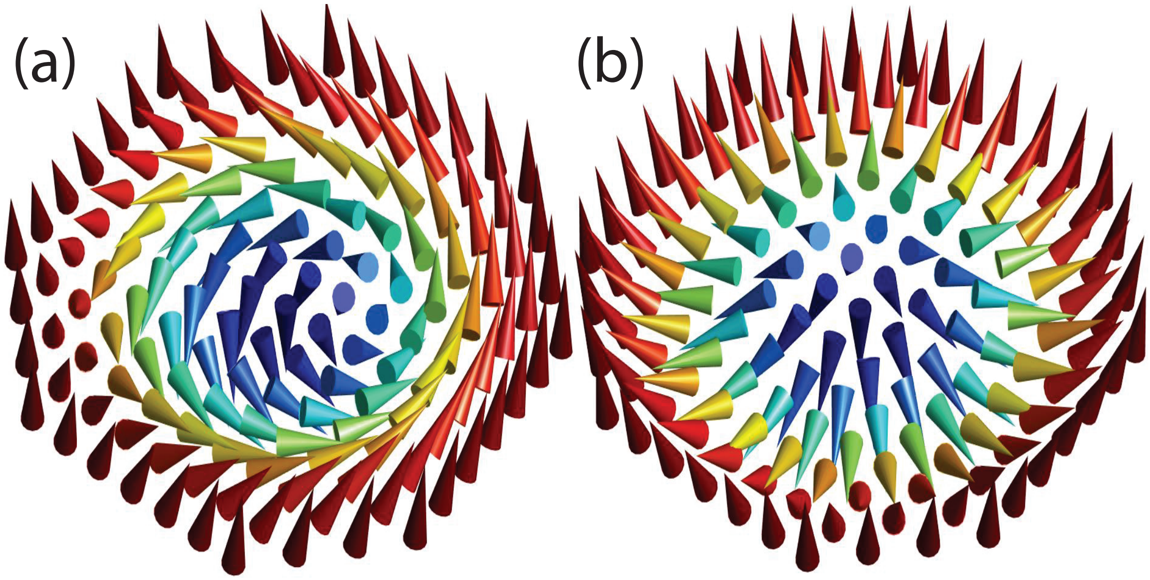

Figure 4.1: The skyrmion texture which is used for our calculation. The skyrmion in Fig. (a), Fig. (b) represents a Bloch ($m = 1, \beta = \pi/2$), a Néel ($m = 1, \beta = 0$) type skyrmion respectively.

4.1 Model

We start with a free-electron system on the surface of TI coupled with the background spin texture of SkX by Hund's rule coupling constant J_H. Our model of topological insulator surface state describes the low lying effective model for bulk Bi_2Se_3, in which the surface states consist of a single Dirac cone at the Γ point [126, 127]. We assume periodic boundary condition in both x and y direction of a square unit cell consisting of 50 lattice sites. We start with the k.p Hamiltonian of a thin layer of three dimensional topological insulator as

$$H_0(\boldsymbol{k}) = h_D(\boldsymbol{k})\tau_z + m_k\tau_x \tag{4.1}$$

where τ_i acts on the surface (top/bottom) and σ_i acts on the spin. In Eq. (4.1), $h_D(\boldsymbol{k}) = v(k_y\sigma_x - k_x\sigma_y)$ is the two-dimensional Dirac cone Hamiltonian with Fermi velocity v, $m_k = m_0 + m_1(k_x^2 + k_y^2)$ represents hybridization between top and bottom surfaces. For our simulation, $m_0 = 6$ meV, $m_1 = 0.2\ \text{eVÅ})^2$, $v = 1 \times 10^6$ m/s. These values represent material parameters for a five-layer of thin TI film.

This momentum space Hamiltonian is transformed into a real space tight binding Hamiltonian by replacing $\mathbf{k}$ with $-i\nabla$ and the differential operators are discretized in a rectangular lattice using finite difference to obtain lattice Hamiltonian

$$\begin{aligned} H = &\sum_i c_i^\dagger \tilde{h_i} c_i + \sum_{<i,j>} (c_i^\dagger t c_j + h.c.) \\ &+ J_H \sum_i c_i^\dagger \boldsymbol{\sigma}_i \cdot \boldsymbol{S}_i c_i. \end{aligned} \tag{4.2}$$

Here $\tilde{h_i}$ is the on-site 4×4 matrix block given as

$$\tilde{h_i} = \begin{bmatrix} 0 & I_1 \\ I_1 & 0 \end{bmatrix} \tag{4.3}$$

where $I_1 = (m_0 + \frac{4m_1}{a^2})I_{2\times 2}$ and $a = 10$Å is the discretization length. The nearest neighbor hopping in the x and y direction becomes

$$t_x = \begin{bmatrix} \frac{iv}{2a}\sigma_y & \frac{-m_1}{a^2}I_{2\times 2} \\ \frac{-m_1}{a^2}I_{2\times 2} & \frac{-iv}{2a}\sigma_y \end{bmatrix}, \tag{4.4}$$

$$t_y = \begin{bmatrix} \frac{-iv}{2a}\sigma_x & \frac{-m_1}{a^2}I_{2\times 2} \\ \frac{-m_1}{a^2}I_{2\times 2} & \frac{iv}{2a}\sigma_x \end{bmatrix}. \tag{4.5}$$

$\boldsymbol{S_i}$ is the onsite spin originating from the skyrmion texture. The interaction between $t_{x,y}$ and J_H dictates the influence of the skyrmion on the anomalous Hall conductivity of the TI surface in this model.

The magnetization of a single skyrmion can be described as

$$\boldsymbol{S}(\boldsymbol{r}) = (\sin\Theta(\boldsymbol{r})\cos\Phi(\phi), \sin\Theta(\boldsymbol{r})\sin\Phi(\phi), \cos\Theta(\boldsymbol{r})) \tag{4.6}$$

where $\Theta(r=0)=0$, $\Theta(0<r<R_s)=\pi(1-r/R_s)$ and $\Theta(r>R_{sky})=\pi$, where R_s is the Skyrmion radius [29]. $\Phi(\phi)=m\phi+\beta$ and $\phi=\tan^{-1}(y/x)$ and β describes the helicity of the skyrmion. We consider a Bloch ($m=1, \beta=\pi/2$), a Néel ($m=1, \beta=0$) type skyrmion for our calculations. The central spin of the skyrmion is aligned at the center of the unit cell and the magnetization $\boldsymbol{S}(\boldsymbol{r})$ is evaluated at each lattice site i to obtain $\boldsymbol{S_i}$ in Eq. (6.1). The total magnetic flux enclosed in a unit cell is one unit flux quantum, $\phi_0=h/e$, which is independent of the skyrmion radius. The effective magnetic flux is $B_{eff}=-\phi_0/(4R_s^2)$. Once the Berry curvature of the TI-SkX system is known, the Hall conductance is calculated from the Kubo formula [2,90]

$$\begin{aligned}\sigma_{xy} = &-\frac{ie^2}{h}\frac{2\pi}{L^2}\sum_{n,k} f(E_{nk})\times \\ &\sum_{m\neq n}\frac{\langle nk|\frac{\partial H}{\partial k_x}|mk\rangle\langle mk|\frac{\partial H}{\partial k_y}|nk\rangle-(n\leftrightarrow m)}{(E_{nk}-E_{mk})^2}\end{aligned} \tag{4.7}$$

where n and m are band indices and $f(E_{nk})$ represents Fermi distribution function.

4.2 Electronic Structure

The electronic bandstructure for TI-SkX system as shown in Fig. 4.2 is generated using a supercell of size 50 × 50 for a Bloch type Skyrmion ($m=1$ and $\beta=\pi/2$). For our

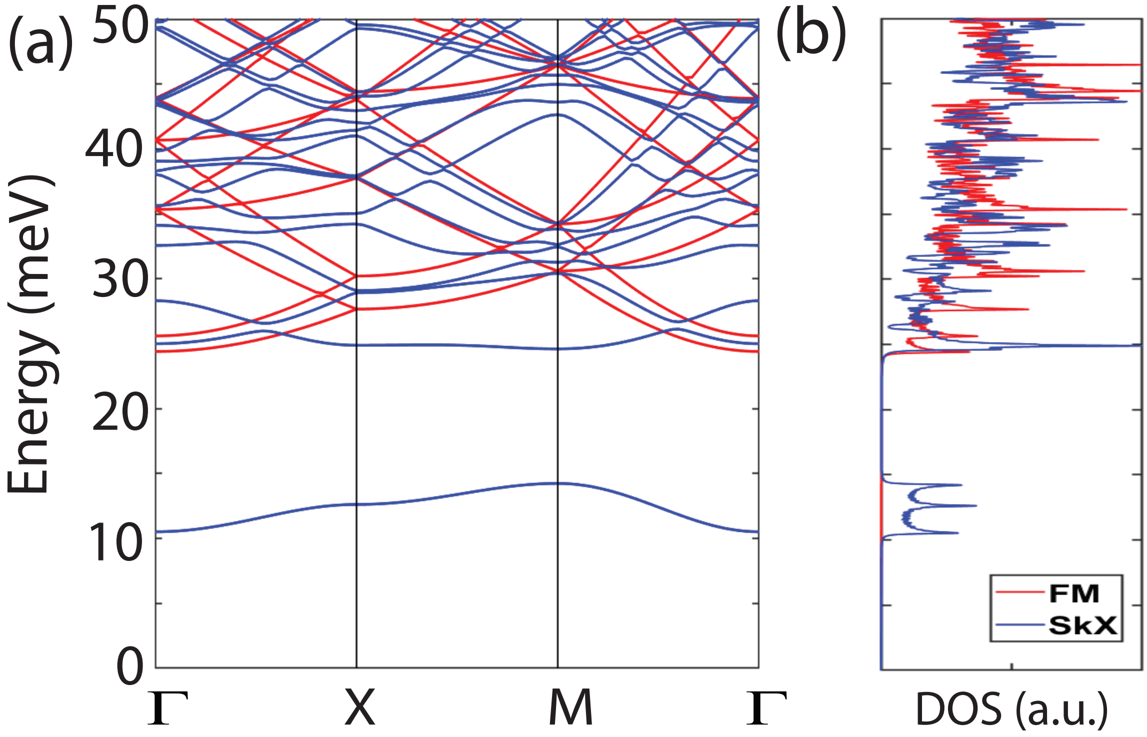

Figure 4.2: The bandstructure and density of state (DOS) of TI surface state in proximity with SkX for $J_H = 25$ meV for a Bloch type Skyrmion with $m = 1, \beta = \pi/2$ and Ferromagnet (FM).

simulation, we consider a thin layer of TI proximity coupled to a SkX layer on the top surface and a ferromagnetic (FM) layer on the bottom surface. The inter site distance between two neighboring lattice points is 10Å. The square Brillouin zone is given by $-\pi/2R_s < k_x, k_y < \pi/2R_s$, where R_s is the skyrmion radius. When $J_H \rightarrow 0$, the TI-SkX system essentially transforms into the TI phase and the energy dispersions form a single Dirac cone in the momentum space. As the value of J_H is increased, the continuous Dirac cone becomes gapped where the value of energy gap is approximately equal to the amount of Hund's exchange coupling constant J_H. As we keep increasing the Hund's exchange coupling parameter J_H, the gap between the electron and hole energy level begins to increase linearly with J_H at first. However, as shown in Fig. 4.2, in addition to one central gap between the electron and hole spectrum, several other energy gaps are also visible from the density of state (DOS) calculation. These energy gaps can be explained by the localized states that are introduced on the surface of TI by skyrmion. Since each skyrmion lives in the ferromagnetic background, when exchange coupled to TI, the ferromagnetic background introduces a finite amount of energy gap in the continuous spectrum of TI. The localized states that form due to the skyrmion reside in this ferromagnetic energy gap and since there is a finite amount of coupling between the localized states of different skyrmions, these bound states form a miniband like dispersion. The magnetic texture of skyrmions leads to the confinement of Dirac states at the skyrmion radius, where the in-plane component of the magnetization vanishes.

Next, we calculate the evolution of the energy gaps as a function of the Hund's rule coupling parameter J_H. Fig. 4.3 shows how the energy gaps change with J_H over a wide range. Here we calculate the energy bandstructure over the whole Brillouin zone and to visualize the gap for each J_H, we collapse all the energy levels over the whole Brillouin zone onto a single vertical line for each value of J_H. The results are summarized in Fig. 4.3.

Intuitively, when J_H is strong enough the spin of the hopping electron on the surface of TI is forced to align parallel to skyrmion spin at each site. For strong enough coupling, the effective hopping between site i and site j can be written as $t_{ij}^{eff} = te^{ia_{ij}} \cos \frac{\theta_{ij}}{2}$ where θ_{ij} is the angle between two spins $\boldsymbol{S}_i$ and $\boldsymbol{S}_j$ at site i and j [128] . For a very strong amount of coupling when an electron hops along a loop at sites 1 → 2 → 3 → 1, the electron obtains a total phase which is equal to the gauge flux a_{ij}. The gauge flux a_{ij} is equal to the one half of the solid angle subtended by the spins at site $1, 2, 3$. This effect is known as spin chirality which is absent for collinear and coplanar spin aligned systems [129, 130]. However, as the amount of the exchange coupling changes from a very low to a very high value, the effective gauge flux as seen by the electrons on the surface of TI changes.

From Fig. 4.3, we find that the band gaps show a scaling behavior for the double exchange coupling constant J_H. As the value of J_H is increased, the skyrmion spin texture gets strongly imprinted on the Dirac electrons of the TI. However, for bound states the net Berry curvature is zero, so the Chern number for each topological gap remains the same as the Fermi energy is changed across the energy level. The topological phase diagram can be intuitively understood for very low exchange coupling J_H. As $J_H \to 0$, the TI-SkX electronic system is that of the TI alone. As the value of J_H is increased, the Dirac electrons on the TI surface feel an average net magnetic field originating from the skyrmion texture which is similar to the ferromagnetic phase. So, a gap opens up between the electron and hole energy states and the Chern number in this gap becomes 1 similar to the ferromagnetic phase. As the value of J_H is increased, the Dirac electron feels the localized spins the skyrmion texture and the bound states become more stable. As the result, the value of the energy gaps continues to increase as a function of J_H. When Fermi energy lies inside an energy gap, the value of Hall conductance σ_{xy} becomes e^2/h. In Fig. 4.4, we show the evolution of energy bandstructure of TI-SkX system as a function of J_H . For a very small value of J_H, there is a single gap between the electron and hole energy states. The energy bound states start to appear when J_H approximately becomes equal to 20 meV.

4.3 Hall Conductance

We show the Hall conductance for different magnetic textures in the weak coupling limit at zero temperature in Fig. 4.5 as a function of the Fermi energy E_F. Here, all three textures show different behavior. The Hall conductance for the ferromagnetic state vanishes as the Fermi level moves away from the Dirac point whereas the Hall conductance for skyrmion textures becomes more prominent. This can be explained as follows. In the present model for the FM:TI all the high energy states are degenerate and free electron like. Hence, σ_{xy} decreases monotonically with the chemical potential. Whereas, in the case of both Bloch and Neel skyrmions, the high energy states are non degenerate, and the bands are split. This creates additional peaks and valleys in the DOS of the high energy bands which causes sudden jumps as the chemical potential moves through those bands. Lastly, the Hall conductance is different for Bloch and Néel type skyrmions, since their density of states is different above the gap as shown in Fig 4.2. These effects become more prominent if J_H is increased two-fold. This leads to a distinct Hall conductance signature as a function of the chemical potential.

4.4 Effect of Ferromagnetic Background on Phase Diagram

In this section, we discuss the effect of the ferromagnetic background and inter-skyrmion distance on the phase diagram and robustness of the Chern numbers of the TI-SkX system. To simulate this effect, we first consider a supercell with a size of 48x48 where the skyrmion diameter spans the entire unit cell, and then we gradually increase the supercell size to 50x50, 52x52 and 54x54 while keeping the skyrmion diameter fixed. Our results are summarized into Fig. 4.6. The integer Chern numbers in each topologically non-trivial gap are also shown in the Fig. 4.6. For the 50x50 unit cell, the phase diagram is identical to the previous phase diagram shown in Fig. 4.3. As the ferromagnetic background and inter-skyrmion distance are increased, the energy levels evolve in a continuous fashion. First, we notice the energy gaps are stable against the change of inter-skyrmion distance. This is expected since the quasi bound states become more stable as the inter-skyrmion distance increases, and subsequently the interaction in-between the electronic levels decreases. The Chern numbers in the topological gaps do not change, which corroborates the fact that the Hall conductivity in such a system, for a specific value of J_H, is stable over a wide range of parameters.

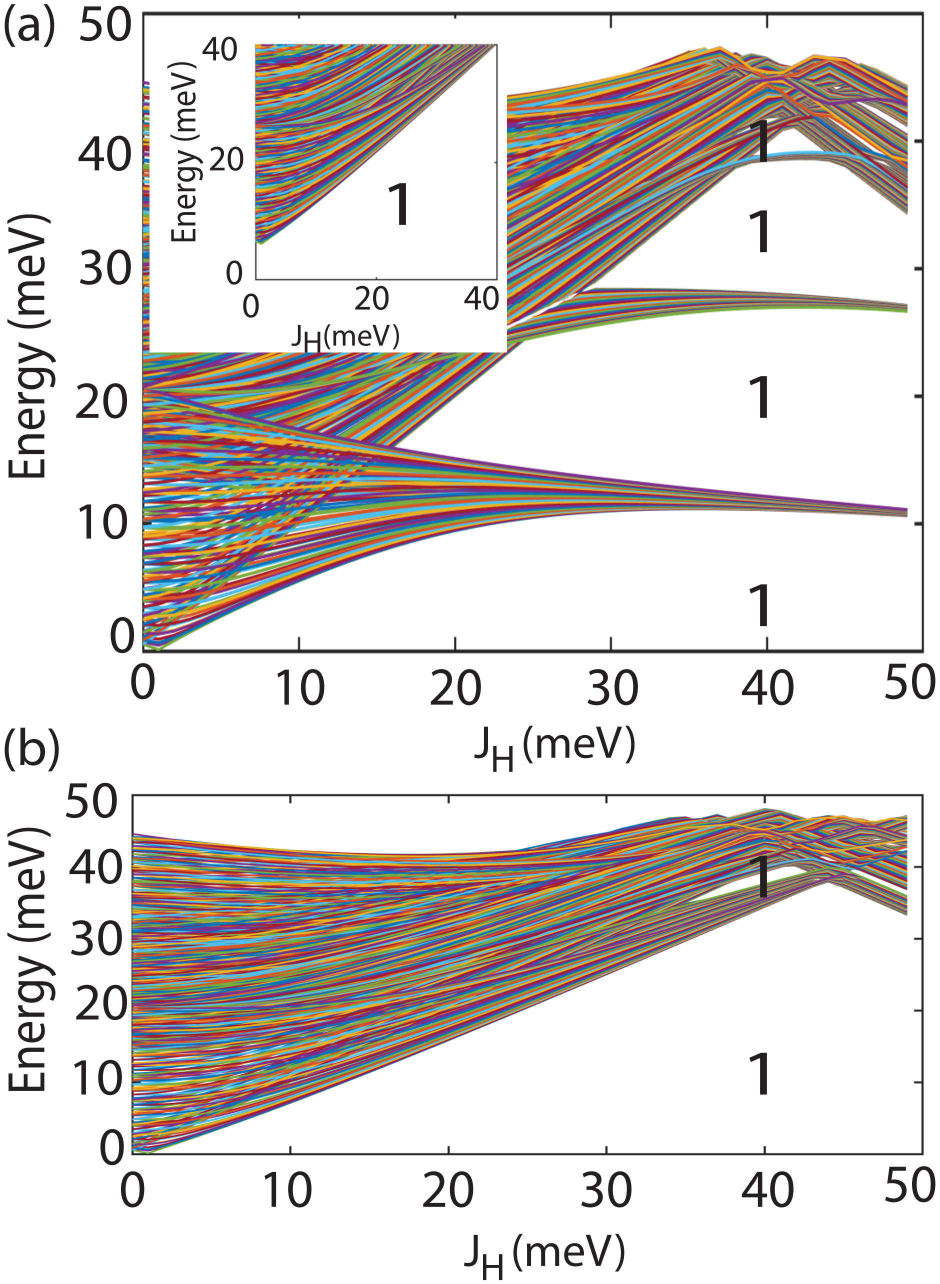

Figure 4.3: Band gaps as a function of J_H for (a) Bloch type and (b) Néel type Skyrmions. The inset shows the phase diagram for the TI-ferromagnetic state. The integer numbers represent the Chern numbers in their corresponding topological gaps.

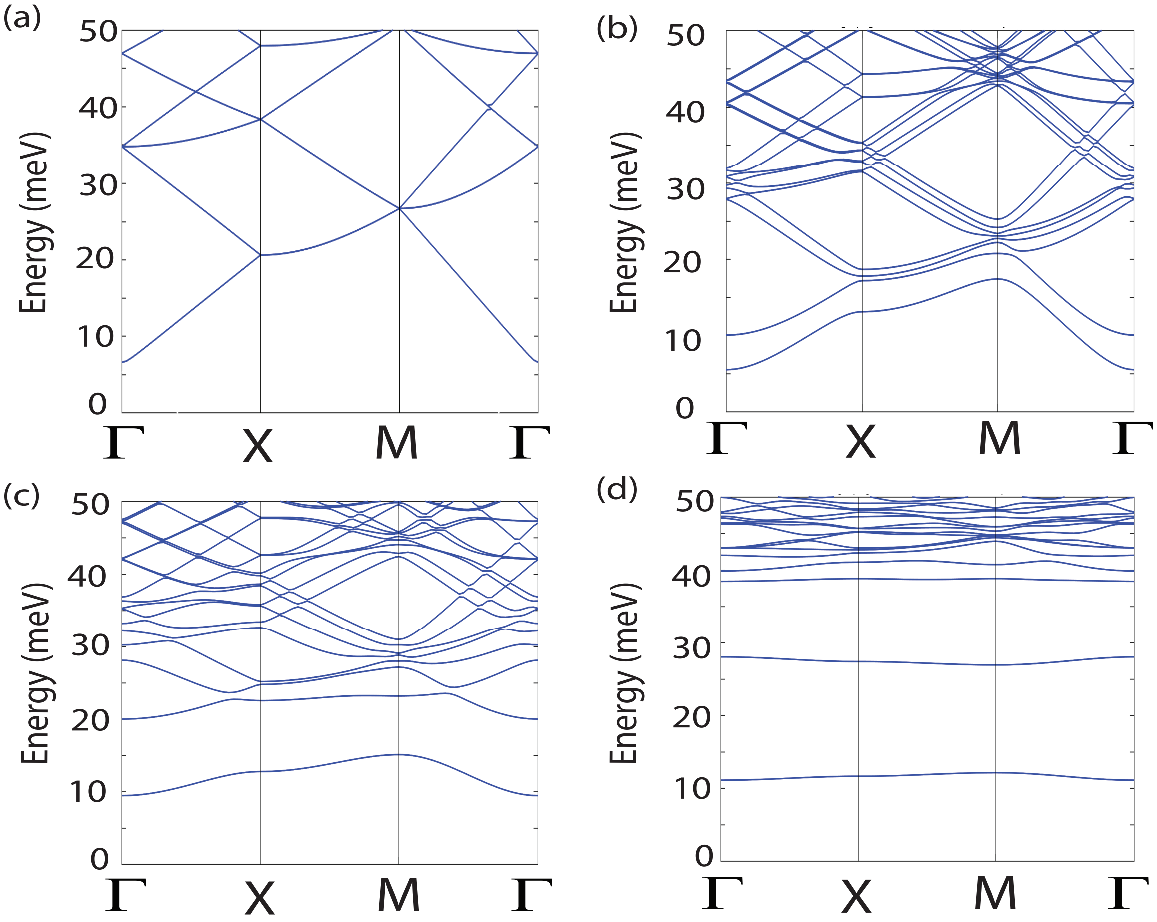

Figure 4.4: Energy bandstructure for TI-SkX system for a Bloch type Skyrmion for different values of J_H of (a) 0 meV, (b) 10 meV, (c) 20 meV, (d) 40 meV.

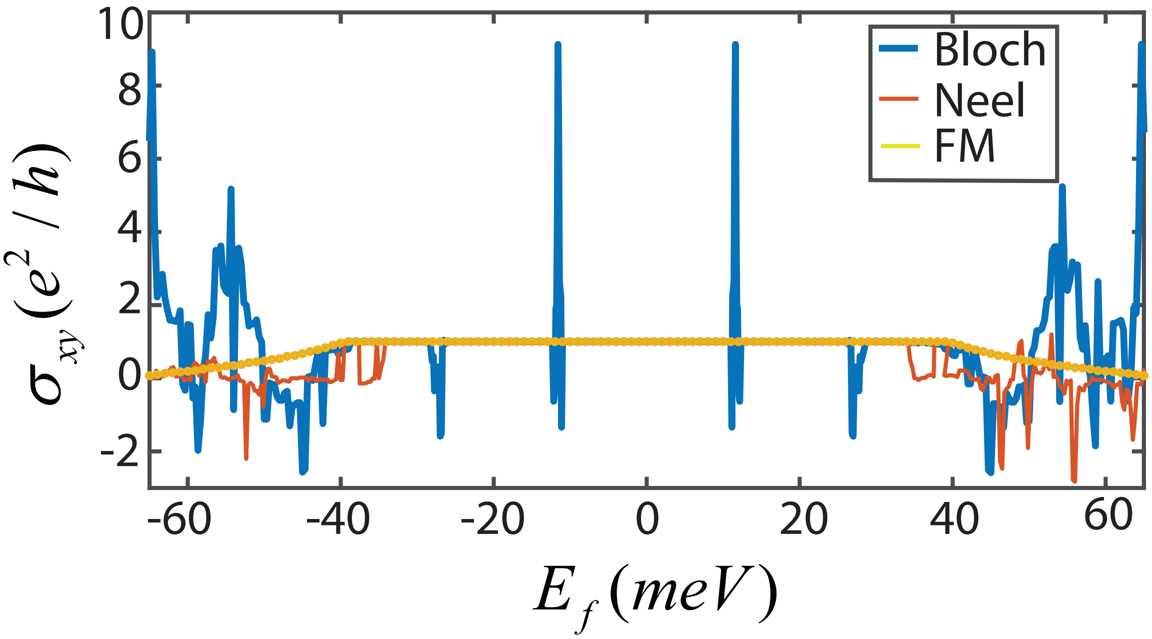

Figure 4.5: The Hall conductance as a function of the Fermi level for different spin textures for $J_H = 40$ meV. Both Bloch and Néel type skyrmions show a distinctive Hall signature as compared to the ferromagnetic state. The Hall conductance is quantized in the energy gap between the electron and hole states.

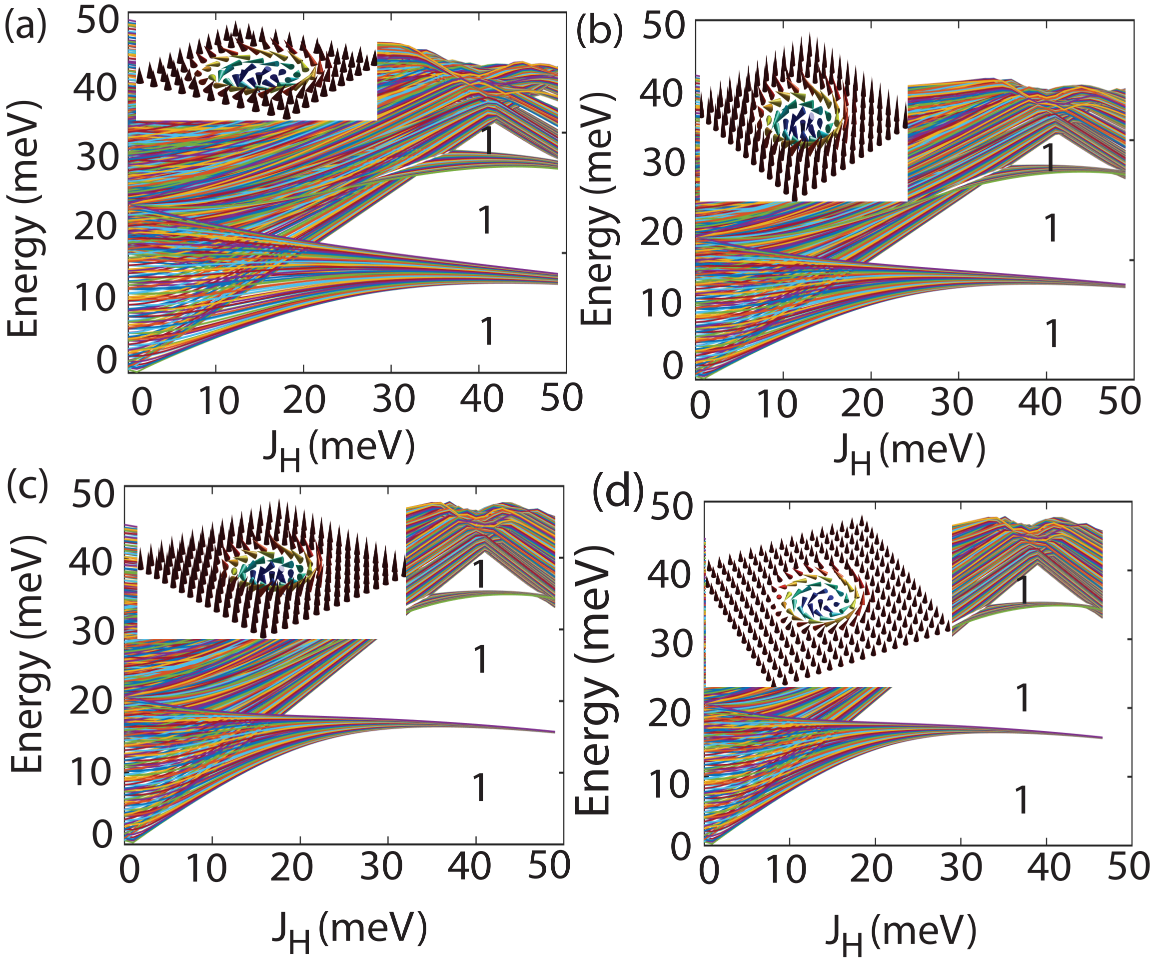

Figure 4.6: The effect of skyrmion radius and ferromagnetic background on the TI-SkX phase diagram. In (a), we show the phase diagram for a skyrmion with a diameter equal to the supercell size 48x48. To simulate the effect of varying ferromagnetic background, we keep the skyrmion radius fixed and gradually increase the supercell size to (b) 50x50, (c) 52x52, and (d) 54x54.

Chapter 5

Dynamics of an Insulating Antiferromagnetic Skyrmion under a Temperature Gradient

A magnetic skyrmion is a non-trivial topological spin texture in which the spins cover the Bloch sphere [13, 87]. They have been demonstrated in both bulk and thin films [12–14]. Magnetic skyrmions have potential applications in energy efficient computing, quantum information processing [87], encoding, transmission, and storage of information [15, 17]. The current required to drive a ferromagnetic skyrmion is $4-5$ orders of magnitude lower than that required to drive a magnetic domain wall [77, 94, 131, 132]. This fact engendered interest in using skyrmions to implement a racetrack memory [16, 17, 133]. Ferromagnetic (FM) skyrmions are sensitive to stray magnetic fields which makes more difficult the reading, writing, and control of an individual skyrmion [17]. When driven by a current in the x-direction, a ferromagnetic skyrmion experiences a Magnus force perpendicular to the applied current resulting in components of the skyrmion velocity in both the x and y direction. This phenomenon is know as the skyrmion Hall effect [134]. For these reasons, there has been a growing interest in the study of antiferromagnetic (AFM) skyrmions.

A g-type antiferromagnetic skyrmion can be viewed as two interleaved pairs of skyrmions of alternate spins. Antiferromagnetic skyrmions are not sensitive to stray fields [135]. They do not posses an intrinsic skyrmion Hall effect, since the skyrmion and the anti-skyrmion exerience equal and opposite Magnus forces. Thus, the velocity of an antiferromagnetic skyrmion is parallel to the driving current [136]. Also, the Dzyaloshinskii-Moriya interaction (DMI) [30], the key ingredient for the formation of skyrmions, is more prevalent in antiferromagnetic (AFM) materials than ferromagnetic (FM) materials [137, 138]. These desireable features have motivated significant interest and recent studies of AFM skyrmions [135, 136, 139–141].

In this article, we investigate the motion of an antiferromagnetic skyrmion in the presence of a a temperature gradient using micromagnetic simulations of the stochastic, lattice Landau-Lifshitz-Gilbert (LLG) equation. Similar to a FM skyrmion, the AFM skyrmion moves from the low temperature region to the high temperature region [142]. The numerical results are well-described by an analytical model. In contrast to the FM skyrmion, an AFM skyrmion has zero average velocity perpendicular to the applied temperature gradient.

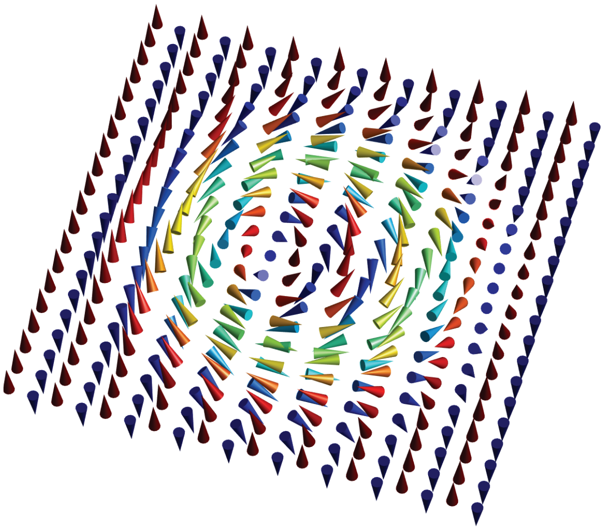

Figure 5.1: A typical spin texture of a G-type Bloch AFM skyrmion which can be thought of as a composite object containing two FM skyrmion with topological charge $+1$ and -1.

5.1 Numerical Simulation

To simulate the magnetization dynamics at finite temperature, the stochastic Landau-Lifshitz-Gilbert (LLG) [143, 144] model is employed. The effect of the thermal fluctuation at temperature T is characterized by a random field $\boldsymbol{L}$. The equation of motion is given by

$$\dot{\boldsymbol{m}} = -\gamma \boldsymbol{m} \times (\boldsymbol{H}_{eff} + \boldsymbol{L}) + \alpha \boldsymbol{m} \times \dot{\boldsymbol{m}} \tag{5.1}$$

where $\gamma = g/\hbar$ is the gyromagnetic ratio, α is the Gilbert damping coefficient, and $\mathbf{m}$ is the magnetization vector whose magnitude is normalized to unity. Since, we consider an AFM skyrmion in an AFM insulator, the damping α is minimal. The effective field acting on the magnetization is determined from the Hamiltonian in the usual manner, $\boldsymbol{H}_{eff} = -\partial \boldsymbol{H}/\partial \boldsymbol{m}$. The stochastic field satisfies the fluctuation-dissipation relationship [145], $< \boldsymbol{L}_u(\boldsymbol{r}, t)\boldsymbol{L}_v(\boldsymbol{r}', t') >= \zeta \delta_{uv} \delta(\boldsymbol{r} - \boldsymbol{r}')\delta(t - t')$, where $\zeta = \alpha a^2 k_B T/\gamma$, a is the lattice constant, and the average is taken over all realizations of the fluctuating field. The stochastic field $\boldsymbol{L}_u(\boldsymbol{r}, t)$ is created with a random number generator with the mean square determined by the temperature, and the stochastic LLG is integrated in the deterministic Heun scheme [142].

The AFM skyrmion system is modeled with the lattice Hamiltonain

$$H = J \sum_{<i,j>} \mathbf{m}_i \cdot \mathbf{m}_j + D \sum_{<i,j>} (\mathbf{u}_{ij} \times \hat{z}) \cdot (\mathbf{m}_i \times \mathbf{m}_j) - K \sum_i (m_z^i)^2. \tag{5.2}$$

The first term is the AFM exchange interaction between two classical spins with AFM exchagne stiffness $J > 0$. The second term is the DMI normal to the plane of the film. The third term is the perpendicular magnetic anisotropy (PMA) with anisotropy constant K and the easy axis perpendicular to the plane of the film. $\sum\limits_{<i,j>}$ is a sum over nearest neighbour sites. The lattice spacing a is 5 Å, and the full simulated grid size is 300 by 100 which is much larger than the AFM skyrmion size ($10a$), so that we can neglect finite size effects. The exchange constant $J = 20.6$ meV, The DMI constant $D = 1.1$ meV, and the perpendicular magnetic anisotropy (PMA) is $K = 93.75$ μeV. These parameters closely resemble the material parameter KMnF$_3$ [146] for which the next-nearest-neighbour (NNN) exchange interaction is much smaller compared to the nearest-neighbour exchange term and has been neglected in our simulation. We use a relatively larger Gilbert damping coefficient $\alpha = 10^{-1}$ which results in a larger stochastic field to more efficiently simulate the AFM skyrmion motion in response to a temperature gradient.

At the beginning of the simulation, the AFM skyrmion starts to move in a Brownian motion type pattern under the influence of the stochastic field. The instantaneous velocity at first looks random, however, as the simulation proceeds, the skyrmion gains

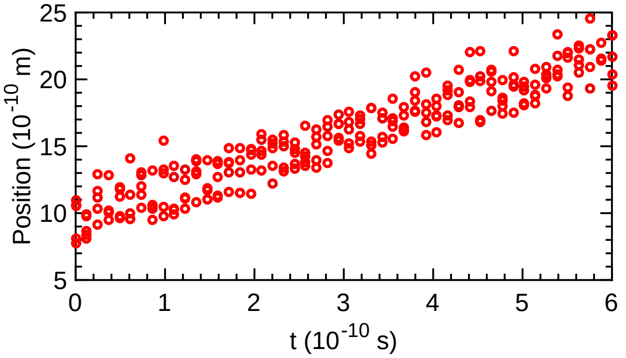

Figure 5.2: Five simulations showing the skyrmions instantaneous longitudinal positions. Although it fluctuates under finite temperature, a forward average velocity is observed.

a net average velocity in a particular direction parallel to temperature gradient. To accurately pinpoint the position of the skyrmion, we define the center of the skyrmion as, $\boldsymbol{r}_c = \int d^2r[\boldsymbol{n} \cdot (\partial_x \boldsymbol{n} \times \partial_y \boldsymbol{n})\boldsymbol{r}] / \int d^2r[\boldsymbol{n} \cdot (\partial_x \boldsymbol{n} \times \partial_y \boldsymbol{n})]$. Since the net topological charge for the AFM skyrmion is zero, to track the skyrmion position the integration has to be performed over the N*é*el vector $\mathbf{n}$ where $\mathbf{n} = \mathbf{m}_1 - \mathbf{m}_2$ and $\mathbf{m}_1$ and $\mathbf{m}_2$ corresponds to the spin texture of each sublattice which is twice the antiferromagnetic order parameter, also known as staggered magnetization, defined as $2\boldsymbol{N} = \boldsymbol{m}_1 - \boldsymbol{m}_2$ [147]. The simulation results are summarized in Fig. 5.2. The skyrmion starts to drift in a particular direction under the influence of the temperature gradient on average on a larger time scale, in a shorter period it seems skyrmion undergoes a Brownian type motion pattern. The velocity is averaged over 50 simulation runs, and its relation with respect to temperature gradient is shown in Fig. 5.3. The longitudinal velocity increases linearly with the temperature gradient. Unlike the FM skyrmion [142], the average transverse velocity of the AFM skyrmion is zero.

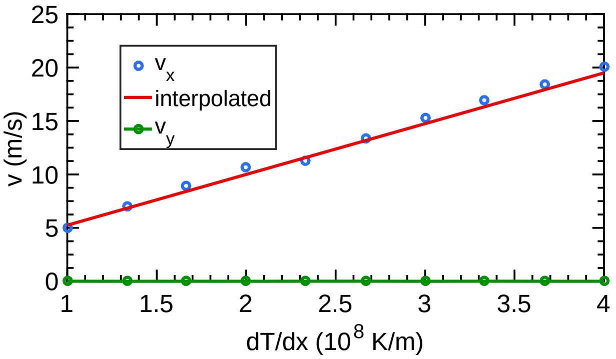

Figure 5.3: A linear scaling between the longitudinal velocity and the temperature gradient is observed from the numerical calculation for $\alpha = 10^{-1}$. Compared to the ferromagnetic skyrmion, a zero transverse velocity is observed, indicating no skyrmion Hall effect in antiferromagnetic case.

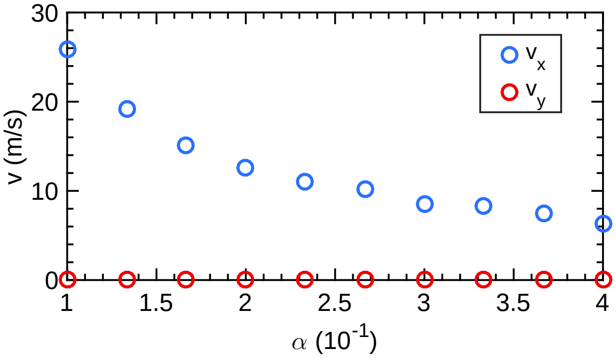

Figure 5.4: The scaling of skyrmion velocity with Gilbert damping α, v_x is inversely proportional to Gilbert damping, whereas the transverse velocity is identically zero.

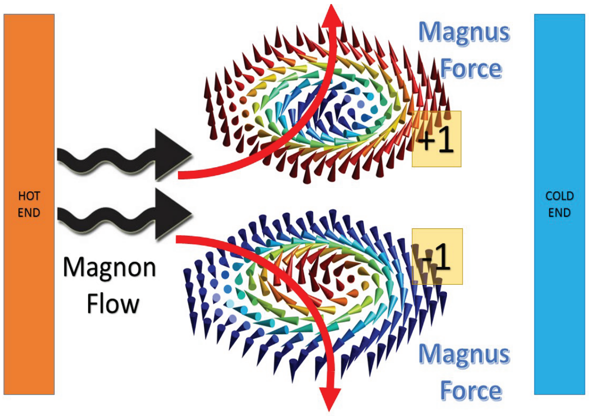

Figure 5.5: The AFM skyrmion is composed of two topological charge +1 and −1; hence, the transverse velocity for each individual particle acts in opposite directions.

5.2 Theory

A theory based on spin wave propagation in a temperature gradient is employed to understand the motion of the AFM skyrmion [142, 144]. We assume each localized spin points in the direction perpendicular to the plane of temperature gradient. The spin's deviation (x, y) from its equilibrium position can be understood from the thermal magnon flow. When a temperature gradient is applied, magnons flow from the high temperature to the low temperature region. The magnon flow provides a negative spin transfer torque on the AFM skyrmion, and since the total angular momentum must be conserved, the skyrmion feels a torque in the opposite direction.

The three dimensional spin texture view of an AFM skyrmion is shown in Fig. 5.1. The topological property can be described in terms of the following equation

$$Q_{AFM} = \int \frac{d^2r}{8\pi} \boldsymbol{n} \cdot (\partial_x \boldsymbol{n} \times \partial_y \boldsymbol{n}) \tag{5.3}$$

where Q_{AFM} corresponds to the AFM skyrmion. For our analysis, we introduce winding number $Q^{(k)}$for each different sublattice as

$$Q^{(k)} = \int \frac{d^2r}{4\pi} \boldsymbol{m}^{(k)} \cdot (\partial_x \boldsymbol{m}^{(k)} \times \partial_y \boldsymbol{m}^{(k)}) \tag{5.4}$$

where $\boldsymbol{m}^{(k)}$ is the unit vector parallel to the local magnetization and $k := \{1, 2\}$ denotes the sublattice. The AFM skyrmion is composed of two topological objects with opposite winding numbers $Q^{(k)} = \pm 1$ which are strongly coupled through the AFM exchange interaction [135].

N$\acute{e}$el vectors in our simulation are initialized parallel to the easy-axis in the z-direction outside the region of skyrmion. Due to the temperature gradient after an initial relaxation, the magnetic moments reach a quasi steady state where the motion of each localized spin becomes time dependent. A linear temperature profile creates a non equilibrium distribution for the magnons, where magnon accumulation is greater in the hotter region compared to the colder one. Since in the hotter region more magnons exist than in the colder one, a net magnon current from the hotter towards the colder region of the system is created which causes deviations of the localized magnetization from the equilibrium value [148–151]. However, the absolute values of the local magnetization is equal for the two sublattices even when a linear temperature profile is assumed. Therefore, the total magnetization in antiferromagnets is compensated and no net magnetization is transferred to the skyrmion [152, 153].

The effect of temperature on the AFM skyrmion can be understood intuitively if we consider how the spin transfer torque arising from the temperature gradient affects each sublattice independently. This concept has also been used to explain the motion of AFM skyrmions in an applied spin polarized current [135]. However, since an AFM skyrmion is a composite object comprising of two ferromagnetic skyrmions in each sublattice, we can assume that the skyrmion in each sublattice interacts with one of the two spin wave modes and since for both of the ferromagnetic skyrmions, the spin wave pushes it to the hotter end, the AFM skyrmion also moves towards the hotter end.

By assuming that an AFM skyrmion is composed of two ferromagnetic skyrmions with topological charge +1 and −1 [142], the following equation for the velocity of an AFM skyrmion has been derived,

$$v_x = \gamma J a^2 j_x - \frac{\gamma}{\pi Q_{(k)}^2} \alpha \eta a^2 k_B T \frac{dT}{dx}, \tag{5.5}$$

where $v_x^M = \gamma J a^2 j_x$ is the AFM skyrmion velocity due to the magnon current, $v_x^B = \frac{\gamma}{\pi Q_{(k)}^2} \alpha \eta a^2 k_B T \frac{dT}{dx}$ is the Brownian part of the motion, and $\eta = (1/8\pi) \int d^2 r (\partial_i \mathbf{m} \cdot \partial_i \mathbf{m})$ is the structure factor [77]. The ratio between the two contributing factors of the velocity is $v^B / v_x^M = (6/\pi) \alpha^2 (D^2 / J k_B T) \approx 10^{-5}$, so the Brownian motion is negligible compared to the magnon driven motion of the skyrmion. Since the transverse velocity, $v_y = 2\alpha \eta v_x^M$, is opposite for the skyrmion and the anti skyrmion, the transverse velocity is negligible.

The magnon current is given by [142] $j_x = -\frac{\pi}{24} a^2 (\frac{k_B}{\hbar s})^2 \frac{T}{\alpha} \frac{dT}{dx}$, where s is the effective magnon velocity, so the magnon current and the skyrmion velocity is proportional to the temperature gradient which is also evident from our numerical simulations. For a magnon velocity $s = 25$ km/s [142], from Eq. (5.5), we get a skyrmion velocity of 4 m/s for a temperature gradient of 10^8 K/m and $\alpha = 0.1$, which closely matches our numerical simulation. It is also evident that j_x is inversely proportional to the Gilbert damping, so the skyrmion longitudinal velocity is dependent on α as is evident from Fig. 5.4.

Chapter 6

Anomalous Magneto Optics from an Antiferromagnet on a Topological Insulator

The Faraday effect and the magneto optic Kerr effect (MOKE), can be viewed as an optical manifestation of the Berry curvature. This is similar to Hall measurements of the topological charge or the Chern numbers.There are however some subtle differences due to the inter- and intra-band transitions, frequency and directional dependence in magneto-optics. Hence magneto optics has been used to study quantum hall effects [39, 154], topological insulators [40, 41, 155], magneto-chiral effects [44], and Hall effects for Skyrmions [45–47, 156].

For electro-optic and memory devices, magneto-electric optical effects can be tremendously useful [42, 43]. MOKE in the polar configuration is particularly interest-

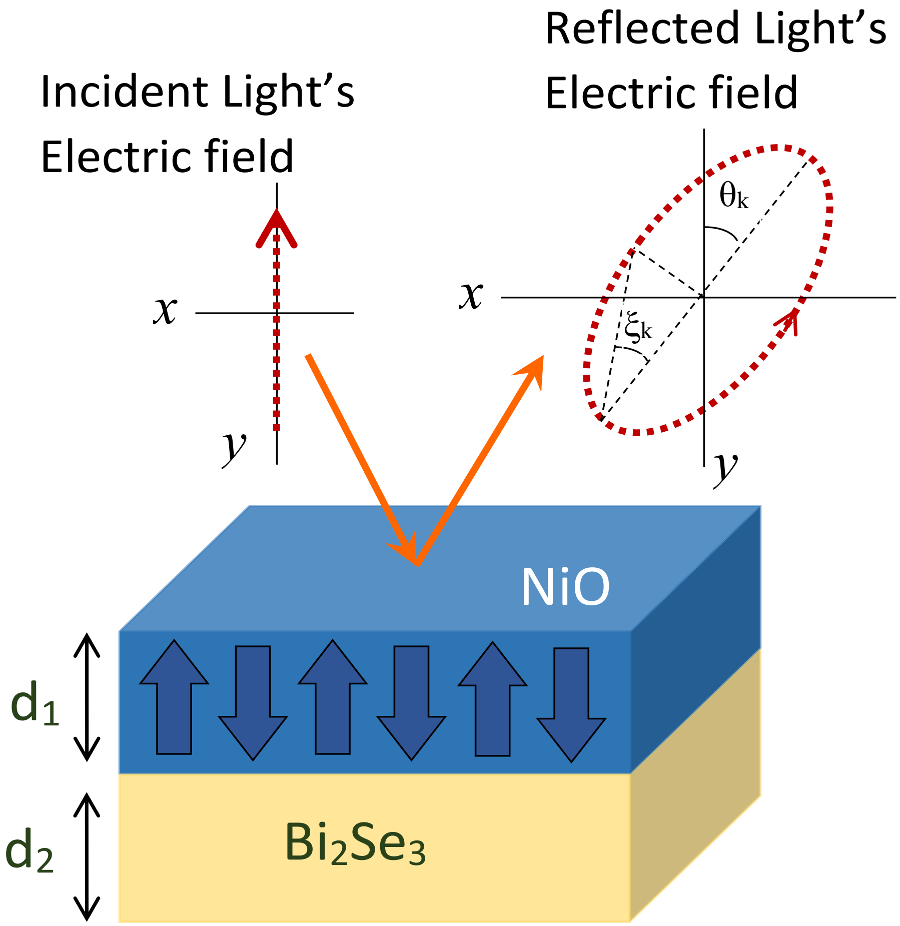

Figure 6.1: MOKE from a thin-film antiferromagnet on top of a thin-film topological-insulator.

ing due to its application in optical reading–out of magnetically stored information [5–7]. However, the thermally–assisted write processes can be relatively slow. For readout, the Kerr rotation is barely one degree for most MO recording materials [51–54, 157, 158], which can result in readout error rates.

Also MOKE requires broken time reversal symmetry (TRS). This is usually done through the application of an external magnetic field. Large and powerful magnets are not particularly useful for miniaturization or and fast device applications. Moreover ferromagnets have slow switching times [159] which makes them poorly suited for high speed magneto-electro-optics. Whereas antiferromagnets (AFM) have been recently shown to have very fast electrical switching times [160]. However a bulk AFM does not give rise to MOKE.

We show that large MOKE signals can be obtained, without an external magnetic field, by combining an AFM with a TI. The AFM microscopically breaks TRS without having a macroscopic magnetic field. We show that the MOKE signal can be further enhanced by cavity resonance effects. We choose NiO for the AFM and Bi_2Se_3 for the TI.

6.1 Model Hamiltonian

The low energy zone-center effective Hamiltonian for a thin-film TI [126, 127] is $H_0(\boldsymbol{k}) = \tau_z h_D(\boldsymbol{k}) + m_k \tau_x$, where τ_z and τ_x are Pauli matrices, respectively representing the TI's top and bottom surfaces and the hybridization between them. $h_D(\boldsymbol{k}) = v(k_y\sigma_x - k_x\sigma_y)$ is the two-dimensional Dirac cone Hamiltonian with Fermi velocity v and $m_k = m_0 + m_1(k_x^2 + k_y^2)$ is the interlayer hybridization. Using $\mathbf{k} \rightarrow -i\nabla$, the following real space tight-binding

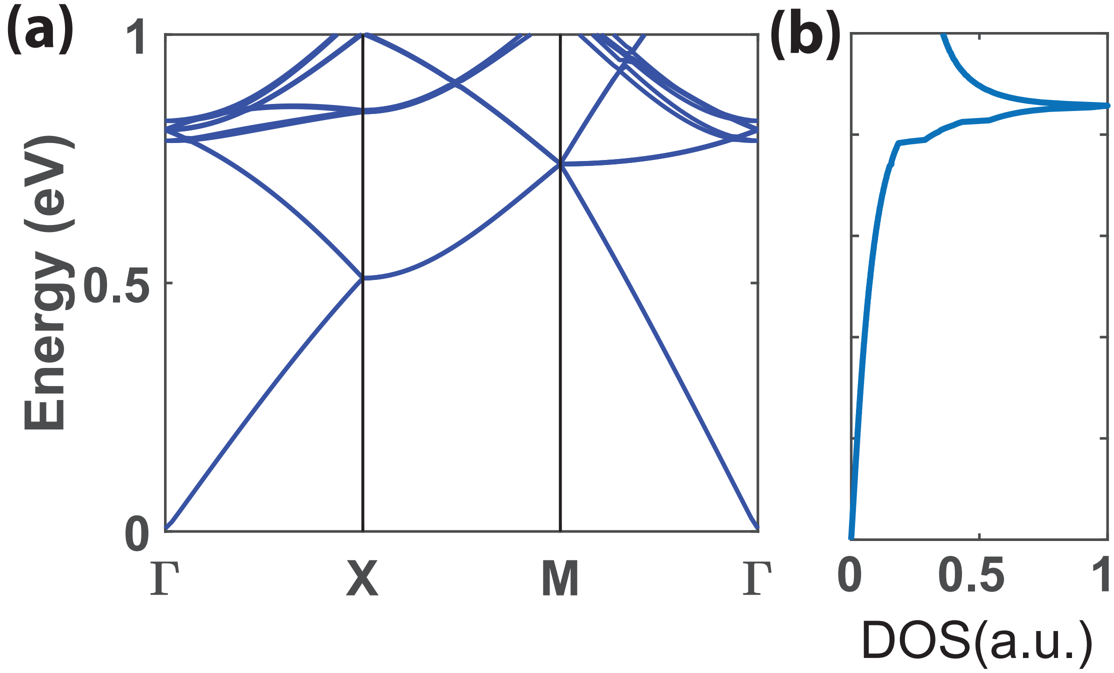

Figure 6.2: Electronic bandstructure and density of states (DOS) for proximity coupled AFM:TI system.

Hamiltonian can be obtained for an AFM proximity coupled to a TI,

$$H = \sum_i c_i^\dagger h_i c_i + \sum_{\langle i,j \rangle} (c_i^\dagger t c_j + h.c.) + J_H \sum_i c_i^\dagger \boldsymbol{\sigma}_i' \cdot \boldsymbol{S}_i c_i. \tag{6.1}$$

where i is the site index and $\langle i, j \rangle$ run over all nearest neighbor sites. Here $t \in \{t_x, t_y\}$ represents nearest neighbor hopping where

$$t_{x(y)} = \pm \frac{iv}{2a} \tau_z \otimes \sigma_{y(x)} - \frac{m_1}{a^2} \tau_x \otimes I \tag{6.2}$$

It is implied that $\boldsymbol{\sigma'} = I \otimes \boldsymbol{\sigma}$, where I is the 2×2 identity, $\boldsymbol{\sigma} = \{\sigma_x, \sigma_y, \sigma_z\}$ is the Pauli spin vector for the TI's itinerant electron and $\boldsymbol{S} = \{S_x, S_y, S_z\}$ is the spin-vector of the AFM. The TI's surface spins are assumed to couple to the AFM's spin via a Hund's rule term J_H. In Eq. (6.2), $h_i = (m_0 + \frac{4m_1}{a^2})\tau_x \otimes I$. We use a 2×2 unit cell assuming periodic boundary conditions along x and y. We set $m_0 = 6$ meV, $m_1 = 0.2$ eVÅ^2, $v = 0.5 \times 10^6$ m/s. The discretization length $a = 10$Å and $J_H = 40$ meV. The band structure of the TI:AFM system is calculated numerically. The electronic bandstructure for TI-AFM system as shown in Fig. 6.2 is generated using a supercell of size 2×2 where the Néel vector of the AFM texture is perpendicular to the TI surface. For our calculation, we consider a thin layer of TI proximity coupled to a G-type AFM layer on the top surface.

Dielectric Tensor Components: Magneto optic effects manifest via the dielectric tensor which depends on the band-structure and its topology. In particular for the polar Kerr effect considered in this paper, the AFM's Néel vector is along z, which is perpendicular to the surface and parallel to the direction of light propagation. The x and y directions preserve in-plane symmetry. The complex 3×3 dielectric tensor has diagonal $[\epsilon_{xx}, \epsilon_{yy}, \epsilon_{zz}]$ terms and the off-diagonal ϵ_{xy} terms which are topology dependent.

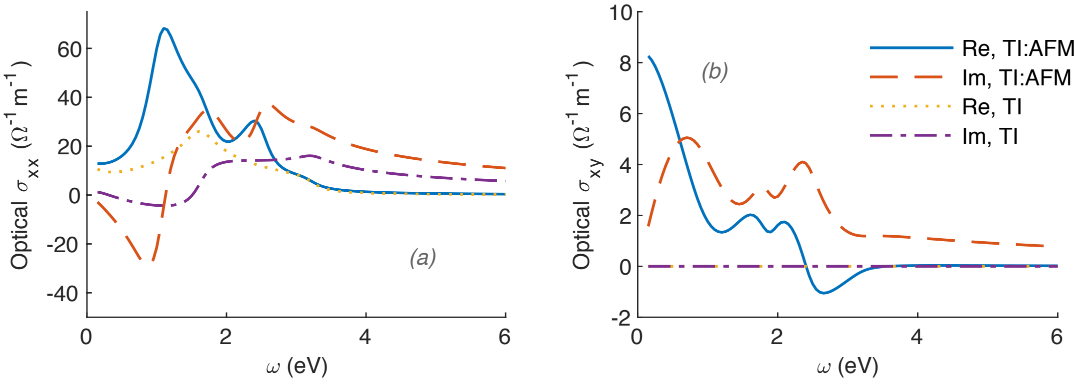

Figure 6.3: Real and imaginary parts of the (a) diagonal- and (b) off-diagonal optical conductivity for just a TI and an AFM on top of a TI.

The matrix elements of the optical conductivity tensor are obtained from the band structure using the Kubo formula [2, 90] as follows,

$$\sigma_{\imath\jmath} = \frac{ie^2}{(2\pi L)^2\hbar} \int \frac{d\boldsymbol{k}}{2\pi} \sum_{n,l} \frac{f_{nl}(\boldsymbol{k})}{\omega_{nl}(\boldsymbol{k})} \left(\frac{\Pi(\boldsymbol{k})^{\imath}_{nl}\Pi(\boldsymbol{k})^{\jmath}_{ln}}{\omega_{nl}(\boldsymbol{k}) - \omega + i\gamma} + \frac{\Pi(\boldsymbol{k})^{\imath}_{ln}\Pi(\boldsymbol{k})^{\jmath}_{nl}}{\omega_{nl}(\boldsymbol{k}) + \omega + i\gamma} \right), \tag{6.3}$$

where $\Pi^{\imath}_{nl}(\boldsymbol{k}) = \langle\psi_n(\boldsymbol{k})|v_{\imath}|\psi_l(\boldsymbol{k})\rangle$ is the velocity operator Here $\{\imath, \jmath\} \in \{x, y\}$, γ is a broadening parameter and $\hbar\omega_{nl}(\boldsymbol{k}) = E_n(\boldsymbol{k}) - E_l(\boldsymbol{k})$, is the energy difference of an optical transition between an unoccupied band, n and an occupied band, l. $f_{nl}(\boldsymbol{k}) = f_n(\boldsymbol{k}) - f_l(\boldsymbol{k})$, where $f_n(\boldsymbol{k})$ is the Fermi filling factor.

Since a low energy effective Hamiltonian has been used to obtain $\sigma_{\imath\jmath}$, the missing higher band contributions in Eq. (6.3) can be included by adding the term $\kappa/(\omega + i\gamma)$. The optical dielectric tensor is then, $\epsilon_{\imath\jmath}(\omega) = \varepsilon_o\delta_{\imath\jmath} - \frac{4\pi i}{\omega}\sigma_{\imath\jmath} - \frac{\kappa}{\omega + i\gamma}$. Here κ is adjusted so that the relative zero frequency dielectric constant ϵ_0 (as obtained from the optical sum rules) matches the known experimental value [91] for Bi_2Se_3. ε_o is the vacuum permittivity.

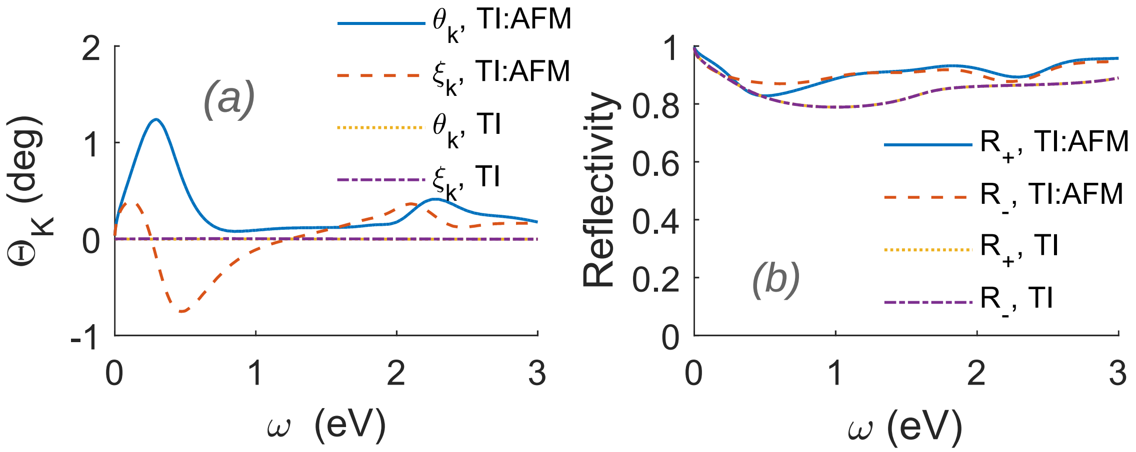

Figure 6.4: (a) Kerr rotation and ellipticity and (b) the reflectivities for a single AFM:TI interface.

6.2 Discussion

The calculated optical dielectric function of the TI with- and without the AFM layer is shown in Fig. 6.3. In case of just the TI, the numerically calculated ϵ_{xy} is zero. This is expected, since the TI preserves TRS. Once an AFM is introduced, the resulting ϵ_{xy} is nonzero.

The resulting Kerr rotations, elipticities and reflectivities for LCP and RCP from this TI:AFM structure are shown in Fig. 6.4 for a single interface. The MOKE resonance, with $\theta_k \approx 1.2^o$ occurs at $\omega(\theta_k^{max})$ in the low energy regime. There is also a high energy MOKE resonance that occurs at the plasma frequency $\omega_p = 2.3$ eV [55, 96, 98], which can be explained with the Drude model [161].

MOKE can be enhanced by the resonance effects that arise from optimizing the film thickness of different materials. In order to understand the effects of this for our system, we consider a thin-film structure as shown in Fig. 6.1 where a NiO film of thickness d_1 sits

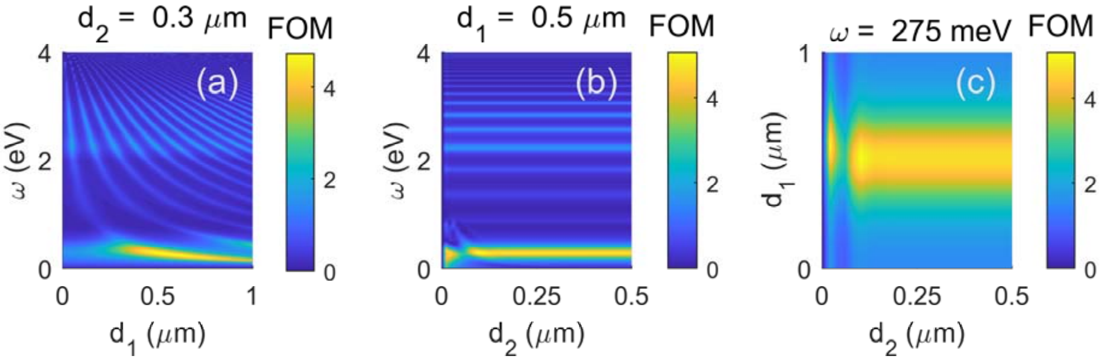

Figure 6.5: The figure-of-merit phase diagram shown as a function of (a) d_1 and ω for $d_2 = 0.3$ μm, (b) d_2 and ω for $d_1 = 0.5$ μm, and (c) d_1 and d_2 for $\omega = 275$ meV.

on a Bi_2Se_3 film of thickness d_2. A 2 × 2 characteristic matrix method [161] was used to calculate the MOKE spectra of multi-layer structure, assuming normal incidence and in-plane material isotropy.

For the TI:AFM device, the FOM phase diagram is shown in Fig. 6.5 as a function of ω, d_1 and d_2. The complete phase space is quite large, therefore representative phase diagrams are shown in Fig. 6.5 where one of the parameters is held constant and the other two are varied. In Fig. 6.5(a) and (b), the FOM is highest for $\omega \sim 275$ meV. Fig. 6.5(a) shows that the FOM has a considerable dependence on the NiO film thickness as the thickness is varied from 0 to 1 μm. Fixing the NiO thickness at 0.5 μm and sweeping the Cu_2OSeO_3 thickness results in a high FOM for a thin 20 nm thickness and also for the thickness of 100 nm or more as shown in Fig. 6.5(b). The FOM phase diagram is shown as a function of d_1 and d_2 in Fig. 6.5(c) for $\omega = 275$ meV. The FOM peaks at $d_1 = 0.5$ μm and $d_2 = 0.1$ μm. The optimum values are obtained from 20 nm or 100+ nm thick Bi_2Se_3 and 500 nm thick NiO for a frequency $\omega = 275$ meV. The MOKE spectra and the reflectivities from 500 nm NiO on 100 nm Bi_2Se_3 are shown in Fig. 6.6. Resonant

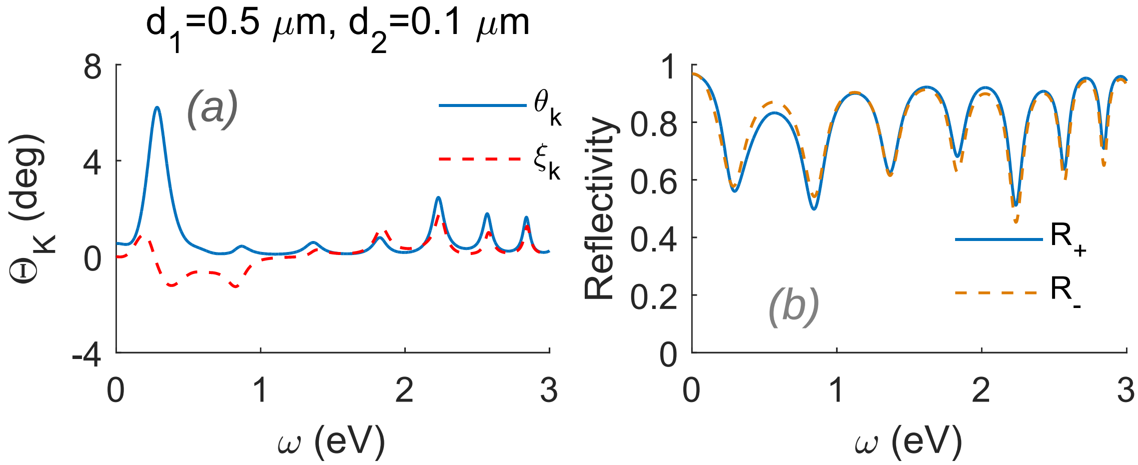

Figure 6.6: (a) Kerr rotation and ellipticity and (b) the reflectivities for a thin-film structure with $d_1 = 0.5$ μm and $d_2 = 0.3$ μm. The MOKE is greatly enhanced because of the resonance effects induced by the thin-film structure.

enhancement resulting from the finite layer thickness increases the Kerr rotation angle from 1.2^o to 6.5^o at the frequency $\omega_r = 275$ meV. Such a large Kerr rotation angle is extremely useful for device applications.

Finally, we calculate Kerr rotation angle as a function of Fermi energy. In Fig. 6.7, the maximum low energy Kerr rotation, θ_k^{max} is shown as a function of Fermi energy E_f. The corresponding ω at which θ_k^{max} occurs is also shown on the right-hand axis. Fig. 6.7(a) shows the dependencies for a single interface, and Fig. 6.7(b) shows the dependencies for the optimum structure of 500 nm NiO on 100 nm Bi_2Se_3 . In both cases, the Kerr rotation angle can be continuously controlled by the Fermi level, and the structure with optimized layer thicknesses increases the range over which the Kerr rotation angle can be swept by sweeping the Fermi energy. This is particulary useful for electro-optic devices such as optical isolators.

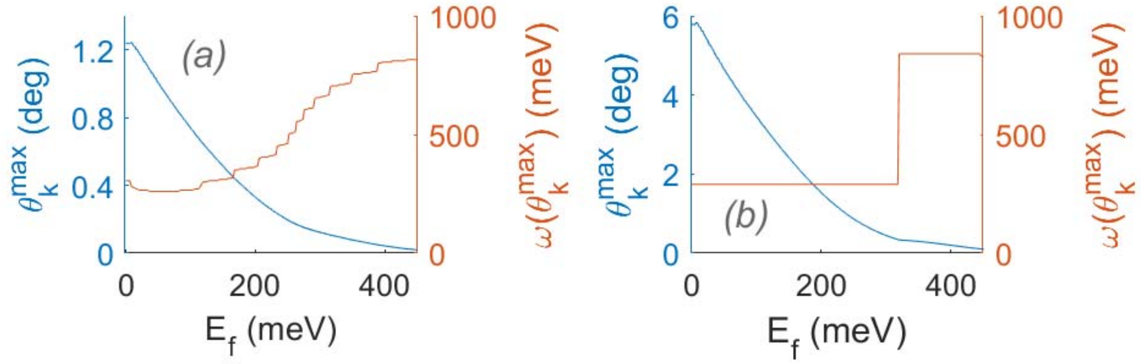

Figure 6.7: The maximum Kerr rotation angle (θ_k^{max}) and the optical frequencies ($\omega(\theta_k^{max})$) at which they occur shown as a function of Fermi energy (E_f) for (a) a single interface and (b) the thin-film structure. θ_k^{max} is distinctly quantized as a function of E_f. These calculations are in the low frequency regime below 1 eV.

Chapter 7

Conclusions

7.1 Magneto Optic Kerr Rotation from Interfacial Topological Insulator-Skyrmion System

The MOKE from SkX-hosting thin-film B20 type compounds interfaced with TI structures displays rich physics with important device applications. High FOM is obtained from the low energy topological MOKE, and the thin-film resonant enhanced MOKE. The MOKE-FOM phase diagram shows that the low energy peaks below the TI's bulk energy gap are large and independent of d_1. For the thin-film induced resonance, the differential MOKE can be large for the FM and SkX states, which is useful for device applications. As E_f is swept above the exchange gap of the surface state, θ_k decreases monotonically for FM:TIs, and it is distinctly oscillatory and non-monotonic for SkX:TIs. These distinguishing $\theta_k(E_f)$ features are not seen for the thin-film induced MOKE resonance.

7.2 Quantized Anomalous Hall Effect in Topological Insulator-Skyrmion Heterostructure

The experimental verification of our proposal is achievable within the regime of current experimental instrumentation. The optimal conditions to detect prefect edge transport associated with the QTHE phase is induced by a skyrmion lattice hosted by an insulating magnetic material that couples electrons of the topological insulator to the skyrmion system. Several ingredients have been already demonstrated in different systems. First, one can use a TI material such as Bi_2Se_3 as a substrate and epitaxially grow another skyrmion hosting material such as Cu_2OSeO_3 on top of it [82]. Second, one can also deposit monolayer of ferromagnet, such as YIG, on topological insulator [162, 163]. The interfacial DM interaction generated as a result of symmetry breaking and high spin orbit coupling originating from TI would generate a skyrmion [27]. Also skyrmion formation has been experimentally demonstrated for TI heterostructures composed of magnetic TI $Cr_x(Bi_{1-y}Sb_y)_{2-x}Te_3$ and non magnetic TI $(Bi_{1-y}Sb_y)_2Te_3$ where the Fermi energy (E_F) can be precisely controlled in a large energy range by applying an external electric field for a field effect transistor (FET) structure [81]. Given that there are no measurement and ab-initio calculation of J_H for TI-SkX system, we have presented our results for a wide range of J_H. The topological phase transitions would take place for a Hund's rule double exchange coupling energy of $J_H = 20$ meV. It has been shown experimentally that a skyrmion forms at the interface of $(Bi_{1-y}Sb_y)_2Te_3$ (BST) and $Cr_x(Bi_{1-y}Sb_y)_{2-x}Te_3$ (CBST) [81]. For this kind of material, since a skyrmion forms at the interface of the heterostructure and in very close proximity with the TI, the Hund's rule coupling energy between the TI and the skyrmion texture would be large. In a TI, the anomalous Hall conductivity arises due to the nonzero Berry curvature in the momentum space. The nonzero Berry curvature can arise due to intrinsic spin-orbit coupling where a topologically nontrivial magnetic texture is not required. In such a case, when time reversal symmetry is broken by a ferromagnet, the quantum anomalous Hall conductivity is realized. The topological Hall effect, also known as geometric Hall effect, can also arise due to the nontrivial topology in real space for which spin-orbit interaction is not required. We have shown that reasonably weak proximity coupling of the skyrmion lattice to the topological insulator would drive the system to a topologically protected quantized topological hall state with multiple gaps, which is distinct from the ordinary anomalous hall phase where there is only one gap. The Chern number of each electronic band gap would be 1. Thus, each topologically protected gap has chiral edge states. The topology of of the electronic bandstructure is robust for different sizes of skyrmions. The Hall effect also appears when the skyrmion texture is not perfectly formed and even for a distorted skyrmion texture the gaps still emerge. Our proposal is distinct from the previous proposals of QAH phase in topological insulator because here multiple gaps open up, unlike just a single gap from the previous proposals, and no external magnetic field is required acting on the topological insulator.

7.3 Antiferromagnetic Magnon Skyrmion Interaction in a Temperature Gradient

We have shown that an antiferromagnetic skyrmion in a finite temperature gradient will move from low to high temperature as a result of magnon flow in the opposite direction.

Compared to the ferromagnetic counterpart, the AFM skyrmion would move with a slightly higher longitudinal velocity, and the transverse velocity is negligible.

7.4 Anomalous Magneto Optics from an Antiferromagnet on a Topological Insulator

The MOKE from TI-AFM system displays rich physics which can lead to antiferromagnetic memory device applications. Large Kerr rotation angles and FOM are obtained for thin film TI-AFM structures. The Kerr rotation can be tuned continuously as a function of Fermi energy by applying an external gate potential. As E_f is swept away from the Dirac point, θ_k decreases monotonically. This device can be used as a potential antiferromagnetic optical isolator with broad applications in spintronics and electro-optics.

Bibliography

[1] Tonmoy K Bhowmick, Amrit De, and Roger K Lake. High figure of merit magneto optics from interfacial skyrmions on topological insulators. *arXiv preprint arXiv:1805.02799*, 2018.

[2] David J Thouless, Mahito Kohmoto, M Peter Nightingale, and Md den Nijs. Quantized hall conductance in a two-dimensional periodic potential. *Physical Review Letters*, 49(6):405, 1982.

[3] Aires Ferreira, N. M. R. Peres, and A. H. Castro Neto. Confined magneto-optical waves in graphene. *Phys. Rev. B*, 85:205426, May 2012.

[4] Mykhailo Tymchenko, Alexey Yu Nikitin, and Luis Martin-Moreno. Faraday rotation due to excitation of magnetoplasmons in graphene microribbons. *ACS nano*, 7(11):9780–9787, 2013.

[5] Yoshishige Suzuki, Toshikazu Katayama, Sadafumi Yoshida, Kazunobu Tanaka, and Katsuaki Sato. New magneto-optical transition in ultrathin fe(100) films. *Phys. Rev. Lett.*, 68:3355–3358, Jun 1992.

[6] P Hansen. Magneto-optical recording materials and technologies. *Journal of Magnetism and Magnetic Materials*, 83(1-3):6–12, 1990.

[7] MASUD MANSURIPUR. The magneto-optical kerr effect. *Opt. Photon. News*, 11(10):34, Oct 2000.

[8] Lei Bi, Juejun Hu, Peng Jiang, Hyun Suk Kim, Dong Hun Kim, Mehmet Cengiz Onbasli, Gerald F. Dionne, and Caroline A. Ross. Magneto-optical thin films for on-chip monolithic integration of non-reciprocal photonic devices. *Materials*, 6(11):5094–5117, 2013.

[9] Mehmet C Onbasli, Lukáš Beran, Martin Zahradník, Miroslav Kučera, Roman Antoš, Jan Mistrík, Gerald F Dionne, Martin Veis, and Caroline A Ross. Optical and magneto-optical behavior of cerium yttrium iron garnet thin films at wavelengths of 200–1770 nm. *Scientific reports*, 6:23640, 2016.

[10] Guoqiang Yu, Pramey Upadhyaya, Xiang Li, Wenyuan Li, Se Kwon Kim, Yabin Fan, Kin L Wong, Yaroslav Tserkovnyak, Pedram Khalili Amiri, and Kang L Wang. Room-temperature creation and spin–orbit torque manipulation of skyrmions in thin films with engineered asymmetry. *Nano letters*, 16(3):1981–1988, 2016.

[11] S Mühlbauer, B Binz, F Jonietz, C Pfleiderer, A Rosch, A Neubauer, R Georgii, and P Böni. Skyrmion lattice in a chiral magnet. *Science*, 323(5916):915–919, 2009.

[12] XZ Yu, Y Onose, N Kanazawa, JH Park, JH Han, Y Matsui, N Nagaosa, and Y Tokura. Real-space observation of a two-dimensional skyrmion crystal. *Nature*, 465(7300):901–904, 2010.

[13] UK Rößler, AN Bogdanov, and C Pfleiderer. Spontaneous skyrmion ground states in magnetic metals. *Nature*, 442(7104):797–801, 2006.

[14] XZ Yu, N Kanazawa, Y Onose, K Kimoto, WZ Zhang, S Ishiwata, Y Matsui, and Y Tokura. Near room-temperature formation of a skyrmion crystal in thin-films of the helimagnet fege. *Nature materials*, 10(2):106–109, 2011.

[15] J Sampaio, V Cros, S Rohart, A Thiaville, and A Fert. Nucleation, stability and current-induced motion of isolated magnetic skyrmions in nanostructures. *Nature nanotechnology*, 8(11):839–844, 2013.

[16] Xichao Zhang, G P Zhao, Hans Fangohr, J Ping Liu, W X Xia, J Xia, and F J Morvan. Skyrmion-skyrmion and skyrmion-edge repulsions in skyrmion-based racetrack memory. *Scientific Reports*, 5:7643, jan 2015.

[17] Albert Fert, Vincent Cros, and João Sampaio. Skyrmions on the track. *Nature nanotechnology*, 8(3):152–156, 2013.

[18] Joel E Moore and Leon Balents. Topological invariants of time-reversal-invariant band structures. *Physical Review B*, 75(12):121306, 2007.

[19] Xiao-Liang Qi and Shou-Cheng Zhang. The quantum spin hall effect and topological insulators. *Physics Today*, 63(1):33–38, 2010.

[20] Netanel H Lindner, Gil Refael, and Victor Galitski. Floquet topological insulator in semiconductor quantum wells. *Nature Physics*, 7(6):490–495, 2011.

[21] Yasuhiro Hatsugai. Chern number and edge states in the integer quantum hall effect. *Physical review letters*, 71(22):3697, 1993.

[22] Emil Prodan. Robustness of the spin-chern number. *Physical Review B*, 80(12):125327, 2009.

[23] Joel E Moore. The birth of topological insulators. *Nature*, 464(7286):194, 2010.

[24] Liang Fu and Charles L Kane. Superconducting proximity effect and majorana fermions at the surface of a topological insulator. *Physical review letters*, 100(9):096407, 2008.

[25] M Zahid Hasan and Charles L Kane. Colloquium: topological insulators. *Reviews of Modern Physics*, 82(4):3045, 2010.

[26] Tony Hilton Royle Skyrme. A non-linear field theory. In *Proceedings of the Royal Society of London A: Mathematical, Physical and Engineering Sciences*, volume 260, pages 127–138. The Royal Society, 1961.

[27] Stefan Heinze, Kirsten Von Bergmann, Matthias Menzel, Jens Brede, André Kubetzka, Roland Wiesendanger, Gustav Bihlmayer, and Stefan Blügel. Spontaneous atomic-scale magnetic skyrmion lattice in two dimensions. *Nature Physics*, 7(9):713, 2011.

[28] AP Malozemoff and JC Slonczewski. *Magnetic Domain Walls in Bubble Materials: Advances in Materials and Device Research*, volume 1. Academic press, 2013.

[29] Jose L Lado and Joaquín Fernández-Rossier. Quantum anomalous hall effect in graphene coupled to skyrmions. *Physical Review B*, 92(11):115433, 2015.

[30] Ivan A Sergienko and E Dagotto. Role of the dzyaloshinskii-moriya interaction in multiferroic perovskites. *Physical Review B*, 73(9):094434, 2006.

[31] M Heide, G Bihlmayer, and S Blügel. Dzyaloshinskii-moriya interaction accounting for the orientation of magnetic domains in ultrathin films: Fe/w (110). *Physical Review B*, 78(14):140403, 2008.

[32] S Rohart and A Thiaville. Skyrmion confinement in ultrathin film nanostructures in the presence of dzyaloshinskii-moriya interaction. *Physical Review B*, 88(18):184422, 2013.

[33] Oleg A Tretiakov and Ar Abanov. Current driven magnetization dynamics in ferromagnetic nanowires with a dzyaloshinskii-moriya interaction. *Physical review letters*, 105(15):157201, 2010.

[34] Soong-Geun Je, Duck-Ho Kim, Sang-Cheol Yoo, Byoung-Chul Min, Kyung-Jin Lee, and Sug-Bong Choe. Asymmetric magnetic domain-wall motion by the dzyaloshinskii-moriya interaction. *Physical Review B*, 88(21):214401, 2013.

[35] Karin Everschor, Markus Garst, Benedikt Binz, Florian Jonietz, Sebastian Mühlbauer, Christian Pfleiderer, and Achim Rosch. Rotating skyrmion lattices by spin torques and field or temperature gradients. *Physical Review B*, 86(5):054432, 2012.

[36] Antoine Georges and Werner Krauth. Numerical solution of the d= hubbard model: Evidence for a mott transition. *Physical review letters*, 69(8):1240, 1992.

[37] Yan Zhou and Motohiko Ezawa. A reversible conversion between a skyrmion and a domain-wall pair in a junction geometry. *Nature communications*, 5, 2014.

[38] Petar Popčević, Jaćim Jaćimović, Alla Arakcheeva, Krunoslav Prša, Helmuth Berger, Ana Smontara, and Lászlo Forró. Physical and structural properties of incomensurately modulated fe 2-x ge intermetallic. *C-MAC Days2014*, 2014.

[39] IV Kukushkin and VB Timofeev. Magneto-optics of strongly correlated two-dimensional electrons in single heterojunctions. *Advances in Physics*, 45(3):147–242, 1996.

[40] Wang-Kong Tse and A. H. MacDonald. Giant magneto-optical kerr effect and universal faraday effect in thin-film topological insulators. *Phys. Rev. Lett.*, 105:057401, Jul 2010.

[41] Wang-Kong Tse and A. H. MacDonald. Magneto-optical faraday and kerr effects in topological insulator films and in other layered quantized hall systems. *Phys. Rev. B*, 84:205327, Nov 2011.

[42] T Arima. Magneto-electric optics in non-centrosymmetric ferromagnets. *Journal of Physics: Condensed Matter*, 20(43):434211, 2008.

[43] Evangelos Atmatzakis, Nikitas Papasimakis, Vassili Fedotov, Guillaume Vienne, and Nikolay I Zheludev. Magneto-optical response in bimetallic metamaterials. *Nanophotonics*, 7(1):199–206, 2018.

[44] Roberta Sessoli, Marie-Emmanuelle Boulon, Andrea Caneschi, Matteo Mannini, Lorenzo Poggini, Fabrice Wilhelm, and Andrei Rogalev. Strong magneto-chiral dichroism in a paramagnetic molecular helix observed by hard x-rays. *Nature physics*, 11(1):69–74, 2015.

[45] Mircea Vomir, Robin Turnbull, Ipek Birced, Pedro Parreira, Donald A MacLaren, Stephen L Lee, Pascal Andre, and Jean-Yves Bigot. Dynamical torque in co x fe3–x o4 nanocube thin films characterized by femtosecond magneto-optics: A π-shift control of the magnetization precession. *Nano letters*, 16(8):5291–5297, 2016.

[46] Seonghoon Woo, Kyung Mee Song, Xichao Zhang, Yan Zhou, Motohiko Ezawa, Xiaoxi Liu, S Finizio, J Raabe, Nyun Jong Lee, Sang-Il Kim, et al. Current-driven dynamics and inhibition of the skyrmion hall effect of ferrimagnetic skyrmions in gdfeco films. *Nature Communications*, 9(1):959, 2018.

[47] Wanjun Jiang, Xichao Zhang, Guoqiang Yu, Wei Zhang, Xiao Wang, M Benjamin Jungfleisch, John E Pearson, Xuemei Cheng, Olle Heinonen, Kang L Wang, , Yan Zhou, Axel Hoffmann, and Suzanne G. E. te Velthuis. Direct observation of the skyrmion hall effect. *Nature Physics*, 13(2):162, 2017.

[48] M Mansuripur. Figure of merit for magneto-optical media based on the dielectric tensor. *Applied physics letters*, 49(1):19–21, 1986.

[49] William A. Challener. Figures of merit for magneto-optic materials. *Journal of Physics and Chemistry of Solids*, 56(11):1499 – 1507, 1995. Proceedings of the 1994 Conference on Magneto-optic Materials.

[50] Alexander R. Taussig, Gerald F. Dionne, and C. A. Ross. Dependence of faraday rotation and magneto-optical figure of merit on dielectric tensor elements in materials with uniaxial symmetry. *Phys. Rev. B*, 77:012407, Jan 2008.

[51] BM Lairson and BM Clemens. Enhanced magneto-optic kerr rotation in epitaxial ptfe (001) and ptco (001) thin films. *Applied physics letters*, 63(10):1438–1440, 1993.

[52] PG Van Engen, KHJ Buschow, R Jongebreur, and M Erman. Ptmnsb, a material with very high magneto-optical kerr effect. *Applied Physics Letters*, 42(2):202–204, 1983.

[53] K Egashira and T Yamada. Kerr-effect enhancement and improvement of readout characteristics in mnbi film memory. *Journal of Applied Physics*, 45(8):3643–3648, 1974.

[54] W Reim and D Weller. Kerr rotation enhancement in metallic bilayer thin films for magneto-optical recording. *Applied physics letters*, 53(24):2453–2454, 1988.

[55] A. De and A. Puri. Application of plasma resonance condition for prediction of large kerr effects. *Journal of Applied Physics*, 92(9):5401–5408, 2002.

[56] A. De and A. Puri. Kerr-resonance-condition-coupled enhancement in magneto-optic media. *Journal of Applied Physics*, 93(2):1120–1126, 2003.

[57] I Gross, W Akhtar, A Hrabec, J Sampaio, LJ Martínez, S Chouaieb, BJ Shields, P Maletinsky, A Thiaville, S Rohart, et al. Skyrmion morphology in ultrathin magnetic films. *Physical Review Materials*, 2(2):024406, 2018.

[58] Jia Li, A Tan, KW Moon, A Doran, MA Marcus, AT Young, E Arenholz, S Ma, RF Yang, C Hwang, et al. Tailoring the topology of an artificial magnetic skyrmion. *Nature communications*, 5:4704, 2014.

[59] R Tolley, SA Montoya, and EE Fullerton. Room-temperature observation and current control of skyrmions in pt/co/os/pt thin films. *Physical Review Materials*, 2(4):044404, 2018.

[60] Shijiang Luo, Min Song, Xin Li, Yue Zhang, Jeongmin Hong, Xiaofei Yang, Xuecheng Zou, Nuo Xu, and Long You. Reconfigurable skyrmion logic gates. *Nano letters*, 2018.

[61] Akira Tonomura, Xiuzhen Yu, Keiichi Yanagisawa, Tsuyoshi Matsuda, Yoshinori Onose, Naoya Kanazawa, Hyun Soon Park, and Yoshinori Tokura. Real-space observation of skyrmion lattice in helimagnet mnsi thin samples. *Nano letters*, 12(3):1673–1677, 2012.

[62] Xiuzhen Yu, John P DeGrave, Yuka Hara, Toru Hara, Song Jin, and Yoshinori Tokura. Observation of the magnetic skyrmion lattice in a mnsi nanowire by lorentz tem. *Nano letters*, 13(8):3755–3759, 2013.

[63] XZ Yu, Y Onose, N Kanazawa, JH Park, JH Han, Y Matsui, N Nagaosa, and Y Tokura. Real-space observation of a two-dimensional skyrmion crystal. *Nature*, 465(7300):901–904, 2010.

[64] SX Huang and CL Chien. Extended skyrmion phase in epitaxial fege (111) thin films. *Physical review letters*, 108(26):267201, 2012.

[65] Shinichiro Seki, XZ Yu, S Ishiwata, and Y Tokura. Observation of skyrmions in a multiferroic material. *Science*, 336(6078):198–201, 2012.

[66] Masahito Mochizuki. Spin-wave modes and their intense excitation effects in skyrmion crystals. *Phys. Rev. Lett.*, 108:017601, Jan 2012.

[67] Masahito Mochizuki and Yoshio Watanabe. Writing a skyrmion on multiferroic materials. *Applied Physics Letters*, 107(8):082409, 2015.

[68] Niklas Romming, Christian Hanneken, Matthias Menzel, Jessica E Bickel, Boris Wolter, Kirsten von Bergmann, André Kubetzka, and Roland Wiesendanger. Writing and deleting single magnetic skyrmions. *Science*, 341(6146):636–639, 2013.

[69] Y Nakatani, M Hayashi, S Kanai, S Fukami, and H Ohno. Electric field control of skyrmions in magnetic nanodisks. *Applied Physics Letters*, 108(15):152403, 2016.

[70] Jonathan S White, Ivana Levatić, AA Omrani, N Egetenmeyer, Krunoslav Prša, Ivica Živković, JL Gavilano, J Kohlbrecher, M Bartkowiak, Helmuth Berger, et al. Electric field control of the skyrmion lattice in cu2oseo3. *Journal of Physics: Condensed Matter*, 24(43):432201, 2012.

[71] Wataru Koshibae, Yoshio Kaneko, Junichi Iwasaki, Masashi Kawasaki, Yoshinori Tokura, and Naoto Nagaosa. Memory functions of magnetic skyrmions. *Japanese Journal of Applied Physics*, 54(5):053001, 2015.

[72] Marine Schott, Anne Bernand-Mantel, Laurent Ranno, Stefania Pizzini, Jan Vogel, Hélène Béa, Claire Baraduc, Stéphane Auffret, Gilles Gaudin, and Dominique Givord. The skyrmion switch: turning magnetic skyrmion bubbles on and off with an electric field. *Nano Letters*, 17(5):3006–3012, 2017.

[73] Y Okamura, F Kagawa, S Seki, and Y Tokura. Transition to and from the skyrmion lattice phase by electric fields in a magnetoelectric compound. *Nature communications*, 7:12669, 2016.

[74] Masahito Mochizuki and Yoshio Watanabe. Writing a skyrmion on multiferroic materials. *Applied Physics Letters*, 107(8):082409, 2015.

[75] Niklas Romming, Christian Hanneken, Matthias Menzel, Jessica E Bickel, Boris Wolter, Kirsten von Bergmann, André Kubetzka, and Roland Wiesendanger. Writing and deleting single magnetic skyrmions. *Science*, 341(6146):636–639, 2013.

[76] Karin Everschor, Markus Garst, RA Duine, and Achim Rosch. Current-induced rotational torques in the skyrmion lattice phase of chiral magnets. *Physical Review B*, 84(6):064401, 2011.

[77] Jiadong Zang, Maxim Mostovoy, Jung Hoon Han, and Naoto Nagaosa. Dynamics of skyrmion crystals in metallic thin films. *Physical review letters*, 107(13):136804, 2011.

[78] Wataru Koshibae and Naoto Nagaosa. Creation of skyrmions and antiskyrmions by local heating. *Nature communications*, 5:ncomms6148, 2014.

[79] Pin-Jui Hsu, André Kubetzka, Aurore Finco, Niklas Romming, Kirsten von Bergmann, and Roland Wiesendanger. Electric-field-driven switching of individual magnetic skyrmions. *Nature Nanotechnology*, 12:123–126, 2016.

[80] Gen Yin, Yufan Li, Lingyao Kong, Roger K Lake, Chia-Ling Chien, and Jiadong Zang. Topological charge analysis of ultrafast single skyrmion creation. *Physical Review B*, 93(17):174403, 2016.

[81] K Yasuda, R Wakatsuki, T Morimoto, R Yoshimi, A Tsukazaki, KS Takahashi, M Ezawa, M Kawasaki, N Nagaosa, and Y Tokura. Geometric hall effects in topological insulator heterostructures. *Nature Physics*, 12(6):555, 2016.

[82] Hilary M Hurst, Dmitry K Efimkin, Jiadong Zang, and Victor Galitski. Charged skyrmions on the surface of a topological insulator. *Physical Review B*, 91(6):060401, 2015.

[83] Hai-Zhou Lu, Wen-Yu Shan, Wang Yao, Qian Niu, and Shun-Qing Shen. Massive dirac fermions and spin physics in an ultrathin film of topological insulator. *Physical review B*, 81(11):115407, 2010.

[84] Y Xia, Dong Qian, David Hsieh, L Wray, A Pal, Hsin Lin, Arun Bansil, DHYS Grauer, YS Hor, RJ Cava, et al. Observation of a large-gap topological-insulator class with a single dirac cone on the surface. *Nature Physics*, 5(6):398–402, 2009.

[85] Leonard Susskind. Lattice fermions. *Physical Review D*, 16(10):3031, 1977.

[86] Seokmin Hong, Vinh Diep, Supriyo Datta, and Yong P Chen. Modeling potentiometric measurements in topological insulators including parallel channels. *Physical Review B*, 86(8):085131, 2012.

[87] Naoto Nagaosa and Yoshinori Tokura. Topological properties and dynamics of magnetic skyrmions. *Nature nanotechnology*, 8(12):899–911, 2013.

[88] Keita Hamamoto, Motohiko Ezawa, and Naoto Nagaosa. Quantized topological hall effect in skyrmion crystal. *Physical Review B*, 92(11):115417, 2015.

[89] N Kanazawa, M Kubota, A Tsukazaki, Y Kozuka, KS Takahashi, M Kawasaki, M Ichikawa, F Kagawa, and Y Tokura. Discretized topological hall effect emerging from skyrmions in constricted geometry. *Physical Review B*, 91(4):041122, 2015.

[90] Mahito Kohmoto. Topological invariant and the quantization of the hall conductance. *Annals of Physics*, 160(2):343–354, 1985.

[91] M Eddrief, F Vidal, and B Gallas. Optical properties of bi2se3: from bulk to ultrathin films. *Journal of Physics D: Applied Physics*, 49(50):505304, 2016.

[92] A Jackson, AD Jackson, and V Pasquier. The skyrmion-skyrmion interaction. *Nuclear Physics A*, 432(3):567–609, 1985.

[93] W Münzer, A Neubauer, T Adams, S Mühlbauer, C Franz, F Jonietz, R Georgii, P Böni, B Pedersen, M Schmidt, et al. Skyrmion lattice in the doped semiconductor fe 1- x co x si. *Physical Review B*, 81(4):041203, 2010.

[94] XZ Yu, N Kanazawa, WZ Zhang, T Nagai, T Hara, K Kimoto, Y Matsui, Y Onose, and Y Tokura. Skyrmion flow near room temperature in an ultralow current density. *Nature communications*, 3:988, 2012.

[95] Petros N. Argyres. Theory of the faraday and kerr effects in ferromagnetics. *Phys. Rev.*, 97:334–345, Jan 1955.

[96] H. Feil and C. Haas. Magneto-optical kerr effect, enhanced by the plasma resonance of charge carriers. *Phys. Rev. Lett.*, 58:65–68, Jan 1987.

[97] A. De and A. Puri. Cyclotron frequency coupled enhancement of kerr rotation in low refractive index-dielectric/magneto-optic bilayer thin-film structures. *Journal of Applied Physics*, 91(12):9777–9787, 2002.

[98] Masanori Abe and Takeshi Suwa. Surface plasma resonance and magneto-optical enhancement in composites containing multicore-shell structured nanoparticles. *Phys. Rev. B*, 70:235103, Dec 2004.

[99] K. H. Miller, X. S. Xu., H. Berger, E. S. Knowles, D. J. Arenas, M. W. Meisel, and D. B. Tanner. Magnetodielectric coupling of infrared phonons in single-crystal $\mathrm{cu_2oseo_3}$. *Phys. Rev. B*, 82:144107, Oct 2010.

[100] Ngoc Han Tu, Yoichi Tanabe, Yosuke Satake, Khuong Kim Huynh, Phuoc Huu Le, Stephane Yu Matsushita, and Katsumi Tanigaki. Large-area and transferred high-quality three-dimensional topological insulator bi2–x sb x te3–y se y ultrathin film by catalyst-free physical vapor deposition. *Nano Letters*, 17(4):2354–2360, 2017.

[101] M Mogi, M Kawamura, R Yoshimi, A Tsukazaki, Y Kozuka, N Shirakawa, KS Takahashi, M Kawasaki, and Y Tokura. A magnetic heterostructure of topological insulators as a candidate for an axion insulator. *Nature Materials*, 16(5):516–521, 2017.

[102] Xiaojun Cheng, Camille Jouvaud, Xiang Ni, S Hossein Mousavi, Azriel Z Genack, and Alexander B Khanikaev. Robust reconfigurable electromagnetic pathways within a photonic topological insulator. *Nature materials*, 15(5):542–548, 2016.

[103] J-C Rojas-Sánchez, S Oyarzún, Y Fu, A Marty, C Vergnaud, S Gambarelli, L Vila, M Jamet, Y Ohtsubo, A Taleb-Ibrahimi, et al. Spin to charge conversion at room temperature by spin pumping into a new type of topological insulator: α-sn films. *Physical review letters*, 116(9):096602, 2016.

[104] J Sánchez-Barriga, A Varykhalov, G Springholz, H Steiner, R Kirchschlager, G Bauer, O Caha, E Schierle, E Weschke, AA Ünal, et al. Nonmagnetic band gap at the dirac point of the magnetic topological insulator (bi1- xmnx) 2se3. *Nature communications*, 7:10559, 2016.

[105] Cui-Zu Chang, Jinsong Zhang, Xiao Feng, Jie Shen, Zuocheng Zhang, Minghua Guo, Kang Li, Yunbo Ou, Pang Wei, Li-Li Wang, et al. Experimental observation of the quantum anomalous hall effect in a magnetic topological insulator. *Science*, 340(6129):167–170, 2013.

[106] Emmanouil Xypakis and Jens H Bardarson. Conductance fluctuations and disorder induced ν= 0 quantum hall plateau in topological insulator nanowires. *Physical Review B*, 95(3):035415, 2017.

[107] Liang Dong, Youngkuk Kim, Dequan Er, Andrew M Rappe, and Vivek B Shenoy. Two-dimensional π-conjugated covalent-organic frameworks as quantum anomalous hall topological insulators. *Physical review letters*, 116(9):096601, 2016.

[108] Xiao Feng, Yang Feng, Jing Wang, Yunbo Ou, Zhenqi Hao, Chang Liu, Zuocheng Zhang, Liguo Zhang, Chaojing Lin, Jian Liao, et al. Thickness dependence of the quantum anomalous hall effect in magnetic topological insulator films. *Advanced Materials*, 28(30):6386–6390, 2016.

[109] Yingfei Gu, Ching Hua Lee, Xueda Wen, Gil Young Cho, Shinsei Ryu, and Xiao-Liang Qi. Holographic duality between (2+ 1)-dimensional quantum anomalous hall state and (3+ 1)-dimensional topological insulators. *Physical Review B*, 94(12):125107, 2016.

[110] T Suzuki, R Chisnell, A Devarakonda, Y-T Liu, W Feng, D Xiao, JW Lynn, and JG Checkelsky. Large anomalous hall effect in a half-heusler antiferromagnet. *Nature Physics*, 12(12):1119–1123, 2016.

[111] Thorsten Hesjedal and Yulin Chen. Topological insulators: Engineered heterostructures. 2016.

[112] Shifei Qi, Zhenhua Qiao, Xinzhou Deng, Ekin D Cubuk, Hua Chen, Wenguang Zhu, Efthimios Kaxiras, SB Zhang, Xiaohong Xu, and Zhenyu Zhang. High-temperature quantum anomalous hall effect in n- p codoped topological insulators. *Physical review letters*, 117(5):056804, 2016.

[113] Ken N Okada, Youtarou Takahashi, Masataka Mogi, Ryutaro Yoshimi, Atsushi Tsukazaki, Kei S Takahashi, Naoki Ogawa, Masashi Kawasaki, and Yoshinori Tokura. Observation of topological faraday and kerr rotations in quantum anomalous hall state by terahertz magneto-optics. *arXiv preprint arXiv:1603.02113*, 2016.

[114] Ming-Xun Deng, Wei Luo, WY Deng, MN Chen, L Sheng, and DY Xing. Competing effects of magnetic impurities in the anomalous hall effect on the surface of a topological insulator. *Physical Review B*, 94(23):235116, 2016.

[115] Minoru Kawamura, Ryutaro Yoshimi, Atsushi Tsukazaki, Kei S Takahashi, Masashi Kawasaki, and Yoshinori Tokura. Current-driven instability of quantum anomalous hall effect in ferromagnetic topological insulators. *arXiv preprint arXiv:1706.00716*, 2017.

[116] Amin Maleki Sheikhabadi and Roberto Raimondi. Inverse spin galvanic effect in the presence of impurity spin-orbit scattering: A diagrammatic approach. *Condensed Matter*, 2(2):17, 2017.

[117] Fridrik Magnus, ME Brooks-Bartlett, R Moubah, RA Procter, Gabriella Andersson, TPA Hase, ST Banks, and Björgvin Hjörvarsson. Long-range magnetic interactions and proximity effects in an amorphous exchange-spring magnet. *Nature communications*, 7, 2016.

[118] Papa Birame Ndiaye, Collins Ashu Akosa, and Aurélien Manchon. Topological hall and spin hall effects in disordered skyrmionic textures. *Physical Review B*, 95(6):064426, 2017.

[119] Naoya Kanazawa, Shinichiro Seki, and Yoshinori Tokura. Noncentrosymmetric magnets hosting magnetic skyrmions. *Advanced Materials*, 2017.

[120] C Moreau-Luchaire, C Moutafis, N Reyren, J Sampaio, CAF Vaz, N Van Horne, K Bouzehouane, K Garcia, C Deranlot, P Warnicke, et al. Additive interfacial chiral interaction in multilayers for stabilization of small individual skyrmions at room temperature. *Nature nanotechnology*, 11(5):444–448, 2016.

[121] Patrick M Buhl, Frank Freimuth, Stefan Blügel, and Yuriy Mokrousov. Topological spin hall effect in antiferromagnetic skyrmions. *physica status solidi (RRL)-Rapid Research Letters*, 11(4), 2017.

[122] Davide Maccariello, William Legrand, Nicolas Reyren, Karin Garcia, Karim Bouzehouane, Sophie Collin, Vincent Cros, and Albert Fert. Electrical signature of individual magnetic skyrmions in multilayered systems. *arXiv preprint arXiv:1706.05809*, 2017.

[123] Roméo Juge, Soong-Geun Je, Dayane de Souza Chaves, Stefania Pizzini, Liliana D Buda-Prejbeanu, Lucia Aballe, Michael Foerster, Andrea Locatelli, Tevfik Onur Menteş, Alessandro Sala, et al. Magnetic skyrmions in confined geometries: effect of the magnetic field and the disorder. *arXiv preprint arXiv:1706.01726*, 2017.

[124] Xiuzhen Yu, Daisuke Morikawa, Yusuke Tokunaga, Masashi Kubota, Takashi Kurumaji, Hiroshi Oike, Masao Nakamura, Fumitaka Kagawa, Yasujiro Taguchi, Taka-hisa Arima, et al. Current-induced nucleation and annihilation of magnetic skyrmions at room temperature in a chiral magnet. *Advanced Materials*, 29(21), 2017.

[125] Hongxin Yang, André Thiaville, Stanislas Rohart, Albert Fert, and Mairbek Chshiev. Erratum: Anatomy of dzyaloshinskii-moriya interaction at co/pt interfaces [phys. rev. lett. 115, 267210 (2015)]. *Physical Review Letters*, 118(21):219901, 2017.

[126] Yongxin Zeng, Chao Lei, Gaurav Chaudhary, and Allan H MacDonald. Quantum anomalous hall majorana platform. *Physical Review B*, 97(8):081102, 2018.

[127] Chao-Xing Liu, Xiao-Liang Qi, HaiJun Zhang, Xi Dai, Zhong Fang, and Shou-Cheng Zhang. Model hamiltonian for topological insulators. *Physical Review B*, 82(4):045122, 2010.

[128] Kenya Ohgushi, Shuichi Murakami, and Naoto Nagaosa. Spin anisotropy and quantum hall effect in the kagomé lattice: Chiral spin state based on a ferromagnet. *Physical Review B*, 62(10):R6065, 2000.

[129] V Kalmeyer and RB Laughlin. Equivalence of the resonating-valence-bond and fractional quantum hall states. *Physical Review Letters*, 59(18):2095, 1987.

[130] Patrick A Lee and Naoto Nagaosa. Gauge theory of the normal state of high-t c superconductors. *Physical Review B*, 46(9):5621, 1992.

[131] F Jonietz, S Mühlbauer, C Pfleiderer, A Neubauer, W Münzer, A Bauer, T Adams, R Georgii, P Böni, RA Duine, et al. Spin transfer torques in mnsi at ultralow current densities. *Science*, 330(6011):1648–1651, 2010.

[132] T Schulz, R Ritz, A Bauer, M Halder, M Wagner, C Franz, C Pfleiderer, K Everschor, M Garst, and A Rosch. Emergent electrodynamics of skyrmions in a chiral magnet. *Nature Physics*, 8(4):301–304, 2012.

[133] R Tomasello, E Martinez, R Zivieri, L Torres, M Carpentieri, and G Finocchio. A strategy for the design of skyrmion racetrack memories. *Scientific Reports*, 4:6784, oct 2014.

[134] Junichi Iwasaki, Masahito Mochizuki, and Naoto Nagaosa. Universal current-velocity relation of skyrmion motion in chiral magnets. *Nature communications*, 4:1463, 2013.

[135] Joseph Barker and Oleg A Tretiakov. Static and dynamical properties of antiferromagnetic skyrmions in the presence of applied current and temperature. *Physical review letters*, 116(14):147203, 2016.

[136] Xichao Zhang, Yan Zhou, and Motohiko Ezawa. Antiferromagnetic skyrmion: stability, creation and manipulation. *Scientific reports*, 6, 2016.

[137] I Dzyaloshinsky. A thermodynamic theory of weak ferromagnetism of antiferromagnetics. *Journal of Physics and Chemistry of Solids*, 4(4):241–255, 1958.

[138] Tôru Moriya. Anisotropic superexchange interaction and weak ferromagnetism. *Physical Review*, 120(1):91, 1960.

[139] Xichao Zhang, Motohiko Ezawa, and Yan Zhou. Thermally stable magnetic skyrmions in multilayer synthetic antiferromagnetic racetracks. *arXiv preprint arXiv:1601.03893*, 2016.

[140] Zhaosen Liu and Hou Ian. Numerical studies on antiferromagnetic skyrmions in nanodisks by means of a new quantum simulation approach. *Chemical Physics Letters*, 649:135–140, 2016.

[141] HD Rosales, DC Cabra, and Pierre Pujol. Three-sublattice skyrmion crystal in the antiferromagnetic triangular lattice. *Physical Review B*, 92(21):214439, 2015.

[142] Lingyao Kong and Jiadong Zang. Dynamics of an insulating skyrmion under a temperature gradient. *Physical review letters*, 111(6):067203, 2013.

[143] José Luis García-Palacios and Francisco J Lázaro. Langevin-dynamics study of the dynamical properties of small magnetic particles. *Physical Review B*, 58(22):14937, 1998.

[144] Denise Hinzke and Ulrich Nowak. Domain wall motion by the magnonic spin seebeck effect. *Physical review letters*, 107(2):027205, 2011.

[145] Rep Kubo. The fluctuation-dissipation theorem. *Reports on progress in physics*, 29(1):255, 1966.

[146] SJ Pickart, MF Collins, and CG Windsor. Spin-wave dispersion in kmnf3. *Journal of Applied Physics*, 37(3):1054–1055, 1966.

[147] Severin Selzer, Unai Atxitia, Ulrike Ritzmann, Denise Hinzke, and Ulrich Nowak. Inertia-free thermally driven domain-wall motion in antiferromagnets. *Physical Review Letters*, 117(10):107201, 2016.

[148] Ulrike Ritzmann, Denise Hinzke, and Ulrich Nowak. Propagation of thermally induced magnonic spin currents. *Physical Review B*, 89(2):024409, 2014.

[149] Jiang Xiao, Gerrit EW Bauer, Ken-chi Uchida, Eiji Saitoh, Sadamichi Maekawa, et al. Theory of magnon-driven spin seebeck effect. *Physical Review B*, 81(21):214418, 2010.

[150] Silas Hoffman, Koji Sato, and Yaroslav Tserkovnyak. Landau-lifshitz theory of the longitudinal spin seebeck effect. *Physical Review B*, 88(6):064408, 2013.

[151] SR Etesami, L Chotorlishvili, A Sukhov, and J Berakdar. Longitudinal spin current induced by a temperature gradient in a ferromagnetic insulator. *Physical Review B*, 90(1):014410, 2014.

[152] Ulrike Ritzmann, Denise Hinzke, and Ulrich Nowak. Thermally induced magnon accumulation in two-sublattice magnets. *arXiv preprint arXiv:1609.02161*, 2016.

[153] SM Rezende, RL Rodríguez-Suárez, RO Cunha, AR Rodrigues, FLA Machado, GA Fonseca Guerra, JC Lopez Ortiz, and A Azevedo. Magnon spin-current theory for the longitudinal spin-seebeck effect. *Physical Review B*, 89(1):014416, 2014.

[154] Yuval Ronen, Yonatan Cohen, Daniel Banitt, Moty Heiblum, and Vladimir Umansky. Robust integer and fractional helical modes in the quantum hall effect. *Nature Physics*, page 1, 2018.

[155] Marc Serra-Garcia, Valerio Peri, Roman Süsstrunk, Osama R Bilal, Tom Larsen, Luis Guillermo Villanueva, and Sebastian D Huber. Observation of a phononic quadrupole topological insulator. *Nature*, 2018.

[156] Wanjun Jiang, Xichao Zhang, Guoqiang Yu, Wei Zhang, Xiao Wang, M Benjamin Jungfleisch, John E Pearson, Xuemei Cheng, Olle Heinonen, Kang L Wang, et al. Direct observation of the skyrmion hall effect. *Nature Physics*, 2016.

[157] P Němec, M Fiebig, T Kampfrath, and AV Kimel. Antiferromagnetic opto-spintronics. *Nature Physics*, page 1, 2018.

[158] RA Duine, Kyung-Jin Lee, Stuart SP Parkin, and MD Stiles. Synthetic antiferromagnetic spintronics. *Nature Physics*, page 1, 2018.

[159] Peter Wadley, Bryn Howells, J Železnỳ, Carl Andrews, Victoria Hills, Richard P Campion, Vit Novák, K Olejník, F Maccherozzi, SS Dhesi, et al. Electrical switching of an antiferromagnet. *Science*, 351(6273):587–590, 2016.

[160] Tomas Jungwirth, X Marti, P Wadley, and J Wunderlich. Antiferromagnetic spintronics. *Nature nanotechnology*, 11(3):231, 2016.

[161] Tonmoy K Bhowmick, Amrit De, and Roger K Lake. High figure of merit magneto optics from interfacial skyrmions on topological insulators. *arXiv preprint arXiv:1805.02799*, 2018.

[162] Xufeng Kou, Liang He, Murong Lang, Yabin Fan, Kin Wong, Ying Jiang, Tianxiao Nie, Wanjun Jiang, Pramey Upadhyaya, Zhikun Xing, et al. Manipulating surface-related ferromagnetism in modulation-doped topological insulators. *Nano letters*, 13(10):4587–4593, 2013.

[163] Ion Garate and Marcel Franz. Inverse spin-galvanic effect in the interface between a topological insulator and a ferromagnet. *Physical review letters*, 104(14):146802, 2010.